The impact of melt ponds on summertime microwave brightness temperatures and sea ice concentrations

S. Kern[1], A. Rösel[2], L.T. Pedersen[3], N. Ivanova[4], R. Saldo[5], and R. T. Tonboe[3]

(1){Center for Climate System Analysis and Prediction CliSAP, Hamburg, Germany}

(2){Norsk Polar Institute, Tromsø, Norway}

(3){Danish Meteorological Institute, Copenhagen, Denmark}

(4){Nansen Environmental and Remote Sensing Center NERSC, Bergen, Norway}

(5){Danish Technical University-Space, Copenhagen, Denmark}

Correspondence to: S. Kern (stefan.kern@uni-hamburg.de)

Abstract

Sea-ice concentrations derived from satellite microwave brightness temperatures are less accurate during summer. In the Arctic Ocean the lack of accuracy is primarily caused by melt ponds but also by changes in the properties of snow and the sea-ice surface between melt ponds. We investigate the sensitivity of eight sea-ice concentration algorithms to melt ponds by comparing sea-ice concentration with melt-pond fraction. We derive gridded daily sea-ice concentrations from microwave brightness temperatures of summer 2009. We derive the daily fraction of melt-ponds, open water between ice floes and ice-surface fraction from contemporary Moderate Resolution Spectroradiometer (MODIS) reflectance. We only use grid cells where MODIS sea-ice concentration, which is melt-pond fraction plus ice-surface fraction, exceeds 90%. For one group of algorithms, e.g., Bristol and Comiso Bootstrap frequency mode (Bootstrap_f), sea-ice concentrations are linearly related to the MODIS melt-pond fraction quite clearly after June. For other algorithms, e.g., Near90GHz and Comiso Bootstrap polarization mode (Bootstrap_p), this relationship is weaker and develops later in summer. We attribute the variation of the sensitivity to the melt-pond fraction across the algorithms to a different sensitivity of the brightness temperatures to snow-property variations. We find an *under-estimation* of the sea-ice concentration by between 14%

1 (Bootstrap_f) and 26% (Bootstrap_p) for 100% sea ice with a melt-pond fraction of 40%. The

2 under-estimation reduces to 0% for a melt-pond fraction of 20%. In presence of *real* open

3 water between ice floes, the sea-ice concentration is *over-estimated* by between 14%

4 (Bootstrap_f) and 26% (Bootstrap_p) at 60% sea-ice concentration and by 20% across all

5 algorithms at 80% sea-ice concentration. None of the algorithms investigated performs best

6 based on our investigation of data from summer 2009. We suggest, that those algorithms

7 which are more sensitive to melt ponds, could be optimized easier because the influence of

8 unknown snow and sea-ice surface property variations is less pronounced.

10 ## 1 Introduction

11 Sea-ice area and extent are derived from data of the sea-ice concentration, i.e. the fraction of a

12 given area of the ocean covered with sea ice. Observations of the brightness temperature by

13 satellite passive microwave sensors have been the backbone for sea-ice concentration retrieval

14 since over 35 years because these are independent of daylight and quite insensitive to the

15 cloud cover. These sensors used for sea-ice concentration retrieval measure the brightness

16 temperature at window frequencies between 6 GHz and ~90 GHz at both, vertical and

17 horizontal polarization, at a constant incidence angle of ~53° which we use for the present

18 paper. Numerous sea-ice concentration retrieval algorithms have been developed during the

19 past decades (see e.g. Ivanova et al., 2015). All algorithms exploit in some way the contrast in

20 the microwave brightness temperature between open water and sea ice to retrieve the sea-ice

21 concentration. During cold conditions, i.e. as long as freezing conditions prevail, sea-ice

22 concentrations are retrieved with these algorithms as accurate as 2% to 5% for the near 100%

23 ice cover (Ivanova et al., 2015, 2014; Andersen et al., 2007; Meier, 2005). However, during

24 melting conditions the retrieval accuracy is reduced substantially and sea-ice concentrations

25 can be biased low compared to the actual sea-ice concentration (Ivanova et al., 2013; Rösel et

26 al., 2012b; Comiso and Kwok, 1996; Cavalieri et al., 1990).

27 One potential reason for the reduced accuracy is the change in microphysical properties inside

28 the sea ice, for instance, the desalination of the sea ice during the melt process or the flushing

29 of air voids in multiyear ice with melt water and other melt processes for example described

30 in Scharien et al. (2010). Another potential reason is the change in surface properties of the

31 sea ice. The three key surface features of summer melt on Arctic sea ice are a metamorphous,

32 wet snow cover, a porous, wet sea-ice surface, and melt ponds. During summer, the snow

33 cover on sea ice is usually wet or even saturated with melt water (Garrity, 1992). Its density is

1   usually considerably larger during summer than during winter (Warren et al., 1999; Maykut

2   and Untersteiner, 1971). Diurnal freeze-thaw cycles, i.e. episodes of intermittent melting and

3   refreezing of the snow, which is a common phenomenon during late spring, result in an

4   increase of the snow grain size.

5   Wet snow is an efficient absorber of microwave radiation and has a microwave emissivity

6   close to 1. It can effectively block microwave emission from underneath and thereby masks

7   differences in volume scattering between first-year and multiyear ice. Therefore microwave

8   brightness temperatures of sea ice covered with wet snow usually are close to its physical

9   temperature during melt (e.g. Stiles and Ulaby, 1980; Eppler et al., 1992; Hallikainen and

10   Winebrenner, 1992; Garrity, 1992).

11   During the thaw phase of freeze-thaw cycles, coarse-grained snow can be regarded to behave

12   similar to wet snow due to its wetness. During the freeze phase, however, when it is dry, it

13   absorbs less microwave radiation than wet snow and there is more scattering from within the

14   snow. Therefore, dry coarse-grained snow does not block or mask microwave emission and

15   volume scattering differences of the sea ice and/or snow underneath as efficiently as wet snow

16   does. The amount of volume scattering depends on microwave frequency and polarization,

17   and on the vertical location of the coarse-grained snow layers relative to the snow surface.

18   Because the electromagnetic wavelengths are closer to the snow grain size at higher

19   frequencies, i.e. at 37-90 GHz, volume scattering in snow is larger for the higher than the

20   lower microwave frequencies (Fuhrhop et al., 1998; Eppler et al., 1992; Hallikainen and

21   Winebrenner, 1992; Gogineni et al., 1992). In Tables 1 to 3 we give sensitivities of brightness

22   temperatures with respect to changes in snow wetness, density, and grain size. These tables

23   are not meant to be exhaustive. Instead we will use the sensitivities for our discussion of the

24   results (section 4).

25   Melt ponds are puddles of melt water on top of sea ice. They form during summer from

26   melting snow and sea ice. Their areal fraction, size and depth is determined by the onset,

27   length and severity of the melting season, the sea-ice type and topography, and the snow-

28   depth distribution at the beginning of melt (Landy et al., 2014; Polashenski et al., 2012;

29   Petrich et al., 2012; Eicken et al., 2004; Perovich et al., 2002). The melt-pond water salinity is

30   close to zero ppt. Typically, the melt-pond fraction on Arctic sea ice varies between 10% and

31   40% but can also exceed 50%, for instance, early in the melt season or on land-fast sea ice

32   (Webster et al., 2015, JGR-O; Divine et al., 2015, TC; Landy et al., 2014; Polashenski et al.,

2012,; Sankelo et al., 2010, POLRES; Tschudi et al., 2001 (JGR-D; Yackel and Barber, 2000; Fetterer and Untersteiner, 1998, JGR-O).

The penetration depth of microwave radiation at the frequencies used here, i.e. between 6 and 89 GHz, into liquid water is in the order of one millimeter (Ulaby et al., 1986). We use the penetration depth here as the depth from which most of the microwave radiation originates. Because of the above-mentioned very low penetration depth, a water layer with a depth of a few millimeters is opaque enough to completely block the microwave signal from the sea ice underneath. A melt pond on sea ice has the brightness temperature signal of open water and is therefore indistinguishable from open water in cracks or leads between the sea-ice floes (Gogineni et al., 1992; Grenfell and Lohanick, 1985). At 6 GHz and higher frequencies the signature of fresh water and salt water are indistinguishable. Satellite microwave sensors which have been used for sea-ice concentration retrieval allow for footprint sizes between ~ 5 km and ~ 70 km. Melt ponds, cracks and leads are therefore sub-footprint size surface features and cannot be resolved individually. A space-borne brightness temperature measurement of a mixed scene is therefore composed of contributions from the open water, i.e. cracks, leads, melt ponds, and from the (snow covered) sea ice. This has two main consequences for a sea-ice concentration product computed from such coarse resolution satellite measurements. The sea-ice concentration in the presence of melt ponds is likely to be underestimated – because melt ponds are seen as open water. Whether the footprint contains, for example, A) 100% sea ice with 40% melt ponds or B) 60% sea ice with 40% open water from leads and openings, is ambiguous. In both cases satellite microwave radiometry retrieves 60% sea-ice concentration because the net sea-ice *surface* fraction of sea ice in the grid cells is 60%. If during summer, a sea-ice concentration retrieval algorithm over-estimates the net sea-ice surface fraction in case A, for example because of a specific summer-time microwave signature of the sea ice, and provides, e.g., ~90% sea-ice concentration, then the same algorithm would most likely also overestimate the net sea-ice surface fraction in case B. The algorithm would hence *under-estimate* the actual sea-ice concentration in case A but *over-estimate* the actual sea-ice concentration in case B.

This has consequences for climate research. For example, the sea-ice area, which is defined as the sum of the area of all sea-ice covered grid cells weighted by the sea-ice concentration, will be computed correctly from case A) but will be under-estimated from case B). Approaches have been developed, which permit to derive the melt-pond fraction on sea ice from satellite observations in the visible/near-infrared frequency range (Istomina et al., 2015a, 2015b; Zege

et al., 2015; Rösel et al., 2012a). Their results could be used to correct the above-mentioned ambiguity by quantifying how much of the open water seen (30% in the example above) is actually caused by melt ponds. However, the time-series of melt-pond fraction data computed so far (2002-2009 and 2002-2011) are too short to apply such a correction for the entire 35 years long sea-ice concentration data set from satellite microwave radiometry. In addition, such data may have limitations due to cloud cover and the viewing geometry at high latitudes (see sub-section 2.1).

The ambiguity in the actual surface properties behind the sea-ice concentration value of 60% in the example above is also challenging for the initialization and evaluation of numerical models, and the assimilation of sea-ice concentration data into such models. An unambiguous sea-ice concentration is required for, e.g., the correct computation of the sea-ice volume. In the terminology of the more advanced thermo-dynamic and dynamic sea-ice models or model components which treat leads and melt ponds separately (e.g. Holland et al., 2012, JC; Flocco et al., 2010, JGR-C), the fraction of sea ice covering the open ocean is called sea-ice concentration and includes melt ponds. The fraction of the latter is given separately as the area of the sea-ice surface covered by melt ponds and is called melt-pond fraction. It is obvious, that such models would have difficulties using a sea-ice concentration product which is biased like described above for cases A and B. Even numerical models, which are not as advanced and which do not treat melt ponds separately, would have difficulties to use such a product.

This calls for a better quantification of the uncertainty and/or of potential biases in the sea-ice concentration. How sensitive are present-day sea-ice concentrations algorithms to the melt-pond fraction? How do these algorithms differ with respect to the expected bias due to melt ponds and how can we explain these differences? We hypothesize that microwave brightness temperatures and sea-ice concentrations derived from them change linearly with the increase in surface-water fraction or the decrease in net sea-ice surface fraction due to melt ponds. To the authors' best knowledge, an inter-comparison of different algorithms which incorporates contemporary information of the melt-pond fraction and an independent sea-ice concentration estimate, as is the aim of this study, has not previously been carried out.

We illustrate how satellite microwave brightness temperature measurements vary with the net sea-ice surface fraction derived from satellite visible/near-infrared (VIS/NIR) imagery. We compare sea-ice concentration obtained with different sea-ice concentration retrieval algorithms from these brightness temperatures with the sea-ice concentration and with the net

sea-ice surface fraction from VIS/NIR imagery. We isolate the influence of melt-pond fractions on the net sea-ice surface fraction by limiting our analysis to VIS/NIR imagery sea-ice concentrations > 90%. We demonstrate how these brightness temperatures change with progression of melt and discuss the implications of this change for sea-ice concentration retrieval.

The paper is organized as follows. The next section (2) describes the data sets and methods used for the inter-comparison of brightness temperatures and sea-ice concentrations derived with several algorithms and the melt-pond fraction. In section 3 we are going to present the results of this inter-comparison which we discuss in section 4. Section 5 concludes the findings.

2   Data and Methods

The paper focuses on the melt season, i.e. months June, July, and August, of the year 2009. The spatial domain of our investigations is a region of the Arctic Ocean (see Figure 1) and it is determined by the area and data which we chose to compute the sea-ice cover parameters from satellite VIS/NIR imagery, described in the following sub-section 2.1.

2.1 Sea-ice parameters from VIS/NIR satellite imagery

2.1.1   Data sets and methodology

We derive the open water fraction, melt-pond fraction, and net sea-ice surface fraction from reflectance measurements of the Moderate Resolution Imaging Spectroradiometer (MODIS) aboard the Earth Observations Satellite TERRA. We use the "*MODIS Surface Reflectance daily L2G Global 500 m and 1 km*" - product (MOD09GA, http://reverb.echo.nasa.gov/reverb/). We obtain the L2G data on the sinusoidal tile grid used for MODIS L2 data from http://modis-land.gsfc.nasa.gov/MODLAND_grid.html. We project the MODIS reflectance data together with land, cloud, and ancillary information onto the NSIDC polar stereographic grid with tangential plane at 70°N with a grid resolution of 0.5 km. Subsequently, we use all re-projected tiles to compose an Arctic mosaic of the MODIS wavelength bands 1: 459-479 nm, 3: 620-670 nm, and 4: 841-876 nm. We apply a spectral un-mixing approach to classify the fractions of open water (between the ice floes), melt ponds, and sea ice, which can be barren or snow covered. For this we use typical reflectance values of these surface types in the above-mentioned wavelength bands (Tschudi et al., 2008). The methodology is explained in more detail together with validation results in Rösel et al.

(2012a) and yields the distribution of the fractions of open water, melt ponds, and net sea-ice surface fraction at 0.5 km grid resolution. We average these distributions onto a NSIDC polar-stereographic grid with 12.5 km grid resolution. Together with the above-mentioned fractions the standard deviation of the melt-pond fraction per grid cell and the number of clear-sky 0.5 km grid cells contributing to each 12.5 km grid cell are stored in netCDF file format. The number of clear-sky grid cells is taken as a measure of the cloud fraction later. The grid resolution of 12.5 km is chosen in accordance to the 8-day MPF data set derived with the same approach but using 8-day composite MODIS reflectance data for years 2000-2011 (Rösel et al., 2012a). We compute the MODIS sea-ice concentration by subtracting the open-water fraction from 100%; note that the MODIS sea-ice concentration includes the sea ice covered by melt ponds while the net sea-ice surface fraction does not. Open-water fraction, melt-pond fraction, and net sea-ice surface fraction add to 100%. For the comparison with the microwave brightness temperatures (sub-section 2.2) and sea-ice concentrations derived from these (sub-section 2.3) we average the MODIS sea-ice parameter data set to 100 km x 100 km grid resolution. In addition, in order to mitigate the influence by variations in the actual sea-ice concentration on our results, we only use grid cells with MODIS sea-ice concentration > 90% unless stated otherwise. Throughout the paper we use the term "ice-surface fraction" for net sea-ice surface fraction.

2.1.2 Quality assessment of the MODIS sea-ice parameters

The quality of MODIS reflectance measurements carried out at high latitudes may be degraded from high sun zenith angles, long pathways through the atmosphere, cloud shadows, and, in addition, shadows caused by ridges in the sea-ice cover. We use only reflectance values with the highest quality score. This ensures that cloudy pixels and pixels with cloud shadows, pixels with sun zenith angles > 85° and pixels with sensor viewing angles > 60°, plus pixels complying with four additional flag criteria are not used.

Mäkynen et al. (2014) hypothesized that our daily MODIS melt-pond fractions are positively biased by about 5-10 % during early melt. In-situ observations carried out north of Greenland revealed a melt-pond fraction of 0% and a sea-ice concentration of 100 % during the first two weeks of June 2009 (Mäkynen et al., 2014). Melt onset dates given in Perovich et al. (2014) support this observation. In order to confirm this notion, we derived histograms of the MODIS melt-pond fraction and the MODIS sea-ice concentration using the data with 12.5 km

grid resolution for latitudes north of 83°N for all days before June 7, 9, 11, and 13, respectively (Figure 2). MODIS melt-pond fractions peak at 8%. There are no grid cells with a melt-pond fraction below 4 %. The MODIS sea-ice concentration peaks at 98 % without any grid cell with values > 98%, suggesting a bias of 2%. We can also confirm the magnitudes of the above-mentioned biases from version 01 of the 8-day MODIS melt-pond fraction product (Kern et al., 2015) and conclude the presence of a systematic bias. Therefore we apply a bias correction and subtract 8% from the melt-pond fractions and add 2% to MODIS sea-ice concentrations. A similar correction (minus 8% and plus 3%) was applied to melt-pond fraction and sea-ice concentration of version 01 of the 8-day MODIS melt-pond fraction product (Rösel et al., 2012a; DOI:10.1594/WDCC/MODIS__Arctic__MPF) yielding version 02: DOI:10.1594/WDCC/MODIS__Arctic__MPF_V02). For the daily product used here, we set the few negative melt-pond fractions resulting from the bias correction to zero.

Even though a state-of-the-art cloud masking scheme has been applied to the MODIS reflectance data before the MODIS sea-ice parameter retrieval (Rösel et al., 2012a), there is still a substantial number of misclassified grid cells. It has been demonstrated that even with a multi-channel instrument such as MODIS, cloud classification is a challenge over bright surfaces such as sea ice or snow (Chan and Comiso, 2013; Karlsson and Dybbroe, 2010). In order to mitigate the influence from misclassifications due to residual clouds, we only use 100 km grid cells with a cloud cover < 5%. About 15 500 grid cells remain for the analysis. We note that for MODIS collection 6 data (we use collection 5) a further improvement of cloud cover properties in the high latitudes is not foreseen (King et al., 2013; Baum et al., 2012) We find that by changing the cloud-cover threshold to 2% or to 10% (not shown), the number of co-located grid cells is changing but the results shown in Section 3 do not. We estimate the average uncertainty in the melt-pond fraction, net sea-ice surface fraction and MODIS sea-ice concentration due to cloud-induced misclassifications to ~ 5%.

More important is the potential misclassification of one of the surface types. The reflectance values used are fixed for the entire summer season and do not take into account the variability in the spectral properties of the melt ponds or the non-ponded sea ice. These spectral properties change as a function of ice type and melt-season duration. The spectral properties of melt ponds are likely to approach those of leads and openings as melt season progresses. This could result in an over-estimation of the melt-pond fraction relative to the open-water fraction or vice versa, because the spectral space between sea ice and water is larger than

between melt ponds and open water (leads). Such a misclassification would have, however, no implications for the net sea-ice surface fraction. It would affect only the melt pond or the open-water fraction.

Rösel et al. (2012a) report RMSD values between MODIS melt-pond fraction and independent melt-pond fraction observations of 4% to 11%. We compare the MODIS sea-ice concentration with visual ship-based sea-ice concentration observations from seven ship expeditions into the Arctic Ocean and obtain an average RMSD of (10.3 ± 3.3)% (range: 6.0% to 15.2%). A comparison of our daily MODIS melt-pond fraction data set with contemporary daily melt-pond fraction estimates based on Envisat MERIS data derived with the approach of Istomina et al (2015a) revealed a consistent agreement (Istomina, Institute of Environmental Physics, University of Bremen, personal communication, May 2016). Based on these results we are quite confident, that the average uncertainty of the melt-pond fraction is better than 10% and that the MODIS ice-surface fraction is as accurate as ~ 5%.

2.2 Satellite microwave brightness temperatures

We use brightness temperatures measured by the Advanced Microwave Scanning Radiometer aboard the Earth Observation Satellite (EOS) TERRA: AMSR-E. The AMSR-E data used are from the 6.9 GHz, 10.7 GHz, 18.7 GHz, 36.5 GHz, and 89.0 GHz channels, which we abbreviate with 6, 10, 19, 37, and 89 GHz henceforth. We take the AMSR-E swath data from the AMSR-E/Aqua L2A Global Swath Spatially-Resampled Brightness Temperatures data set, version 2: http://nsidc.org/data/docs/daac/ae_l2a_tbs.gd.html, (Ashcroft and Wentz, 2013). We resample the brightness temperatures of all channels to the resolution of the 6 GHz channel, which has a 3-dB footprint of 43 km x 75 km, and co-locate these to the MODIS sea-ice parameters provided at 100 km grid resolution (sub-section 2.1). We include data from all AMSR-E passes of the same day as the MODIS data. Only data with footprints which center I located within 5 km of the center of a MODIS sea-ice parameter grid cell are used. AMSR-E sampling is approximately every 10 kilometers so this gives us approximately 1 data point from each AMSR-E pass.

2.3 Sea-ice concentration algorithms

We compute sea-ice concentrations from this set of co-located AMSR-E brightness temperatures (sub-section 2.2) using eight selected sea-ice concentration retrieval algorithms

investigated in the European Space Agency Climate Change Initiative – Sea Ice (SICCI) project. The full suite of SIC algorithms used in the SICCI project is documented in the SICCI project reports: PVASR (Ivanova et al., 2013) and ATBD (Ivanova et al., 2014), where also the open-water and sea-ice tie points can be found. These represent winter conditions. The motivation for this is two-fold. One is our wish to inter-compare the eight algorithms independently of individual tie points being specifically selected in the original algorithms. We want to use *one* universal set of tie points (see also Ivanova et al., 2015). This implies the second reason why we use winter tie points in the present study. For the derivation of the sea-ice tie points Ivanova et al. (2015) used high ice concentration areas of convergent ice motion during winter. This ensures that i) the areas from which tie points are retrieved are large enough and ii) the areas have indeed 100% sea-ice concentration. Such an approach does not work under summer conditions because openings / leads in the ice cover do not freeze over. In the present study we focus on a selected number of different (representative) types of algorithms (Ivanova et al., 2015) and do not include algorithms where a methodology is duplicated. The selected algorithms are summarized in Table 4.

We categorize the algorithms into four types based on the way brightness temperatures are used: 1) algorithms based on one polarization and one frequency (e.g. One_channel 6H); 2) algorithms based on different frequencies but the same polarization such as the frequency mode of the Comiso Bootstrap algorithm (Bootstrap_f); 3) algorithms based on different polarizations but the same frequency such as the polarization mode of the Comiso Bootstrap algorithm (Bootstrap_p); 4) algorithms based on at least two frequencies and/or polarizations like the NASA-Team algorithm (NASA_Team).

A fifth type of algorithms are the so-called hybrid algorithms. These combine two or more of the above-mentioned types of algorithms such like the Eumetsat OSI-SAF algorithm (Eastwood et al., 2012) or SICCI (Ivanova et al., 2015) which combine Bristol and Bootstrap_f, and the Arctic version of the Comiso Bootstrap algorithm (Comiso et al., 1997; Comiso 2009), which combines Bootstrap_f and Bootstrap_p. For the high sea-ice concentrations we focus on in this paper, these two hybrid algorithms are almost identical to the algorithm, which is employed at high sea-ice concentrations, that is Bristol in case of the OSI-SAF and SICCI algorithms and Bootstrap_p in case of the Comiso Bootstrap algorithm. Therefore we do not show the analysis for the hybrid algorithms in this paper.

2.4 Sea-ice age data set

Brightness temperature changes over Arctic sea ice are different for first-year ice (FYI) and multiyear ice (MYI) (Eppler et al., 1992). In order to separate these two sea-ice types we use the Arctic sea-ice age data set (Tschudi et al., 2016). This data set is available with weekly temporal resolution, has a grid resolution of 12.5 km x 12.5 km and is based on sea-ice drift trajectory analysis (Tschudi et al., 2010; Fowler et al., 2003). We prefer this data set over other approaches because the latter are usually limited to the winter period (e.g. Comiso, 2012; Swan and Long, 2012). We co-locate the sea-ice age data set with the MODIS sea-ice parameter data set as follows. For each MODIS data set grid cell we first find the sea-ice age grid cell which center has the smallest distance to the center of the MODIS data set grid cell. Secondly, we select a 7 x 7 grid cell array around that first co-located grid cell from the sea-ice age data set. Subsequently, we count the numbers with which a certain sea-ice age occurs within the co-located 7x7 grid cell array and divide by the total number (for every ice age) of counts. We assign the ice type FYI to the respective MODIS data-set grid cell only if more than 90% of the counts indicate a sea-ice age of 1 year. We correspondingly assign the ice type MYI only if more than 90% of the counts indicate a sea-ice age of 3 years or older. All other grid cells are kept without any classification into an ice type. In our co-located data set, FYI is assigned to MODIS data set grid cells in the northern Chukchi Seas and parts of the central Arctic Ocean as well as north of Franz-Josef Land (Figure 1 a). Multi-year ice is assigned to MODIS data set grid cells north of the Canadian Arctic Archipelago (Figure 1 b). The latter region is also the area where the largest number of co-locations is found whereas only few co-locations are found in the northern Chukchi Sea (Figure 1 c).

3.1 MODIS sea-ice parameters

We show the temporal development of the daily sea-ice parameters obtained with MODIS (subsection 2.1) for June to August 2009 in Figure 3. These include MODIS sea-ice concentration, the net sea-ice surface fraction, the net surface-water fraction, which is the open-water fraction plus the melt-pond fraction, and the melt-pond fraction for each day and each co-located grid cell. No further averaging is applied and we show all grid cells regardless of ice type. Gaps in the time series and the varying number of data points are caused by daily variations in cloud cover and the decrease in sea-ice cover from June to August. Only grid

1 cells with MODIS sea-ice concentration > 90% are shown; the number of grid cells fulfilling

2 this criterion is decreasing with progressing melt season.

3 During the first 2-3 weeks the MODIS melt-pond fraction in our data set remains near zero.

4 Then the melt-pond fraction starts to increase, first slowly: days 20-30 (5th and 6th pentad of

5 June), then rapidly: days 30-45 (1st to 3rd pentad of July). After a short plateau where melt-

6 pond fractions remain near 35% it first declines rapidly to about 20% at days 55-60 (last

7 pentad of July) and then more slowly to about 15% until the end of our study period (Aug.

8 31). Throughout June, MODIS sea-ice concentrations are close to 100% (until day 30), and

9 then there is more variability around 90-95% after day 55. Net total water fraction and net

10 sea-ice surface fraction, are linked to the previous two parameters and add up to 100%.

11 **3.2   AMSR-E sea-ice concentration compared to MODIS sea-ice**

12 **concentration**

13 We first compare sea-ice concentrations derived with the algorithms listed in Table 4 from

14 AMSR-E brightness temperatures (sub-sections 2.2 and 2.3) with MODIS sea-ice

15 concentrations (sub-section 2.1) with the aim to illustrate how summer-time AMSR-E sea-ice

16 concentrations compare to an independent sea-ice concentration estimate. We include all data

17 with MODIS sea-ice concentrations > 20%. We find different agreement between AMSR-E

18 and MODIS sea-ice concentrations for the different algorithms for June (Table 5), July

19 (Figure 4, Table 6) and August (Table 7) of the year 2009. Common to all algorithms is a

20 cluster of data, which is more or less centered at an AMSR-E sea-ice concentration of 100%.

21 Slopes of a linear regression forced through the point (0,0) range from 0.90 for Bootstrap_p

22 (Figure 4 e) to 1.12 for Bootstrap_f (Figure 4 b). Values of the root mean square difference

23 (RMSD) between AMSR-E and MODIS sea-ice concentrations vary between 7.4 % for NT2

24 (Figure 4 f) and 18.1 % for Bootstrap_f. Only few values of MODIS sea-ice concentrations <

25 80% exist. For these, AMSR-E sea-ice concentrations are generally biased low by between 10

26 and 20% - except for the NT2-algorithm (Figure 4 f). The ASI and NT2 algorithms cut off

27 sea-ice concentrations once they exceed 103% and 100% ice concentration, respectively. We

28 exclude these two algorithms therefore out of the following quality ranking.

29 We take the slope (the closer to 1 the better), the correlation (the higher the better) and the

30 RMSD (the lower the better) as a quality measure and find the NASA-Team algorithm to

31 outperform all other algorithms listed in Table 4 for June (Table 5) – no matter whether we

32 use all grid cells or only FYI or MYI grid-cells (see sub-section 2.4). For July (Table 6), the

NASA-Team algorithm is as good as the Near90_lin algorithm. For August (Table 7), best slopes are obtained for the Bootstrap_p algorithm while lowest RMSD values are obtained for the NASA-Team algorithm. Note that the number of FYI grid cells is extremely low for August and that the numbers given in Table 7 for FYI should not be over-interpreted.

The average correlation, computed from six algorithms, decreases from June: 0.72 ± 0.07 over 0.53 ± 0.18 in July to 0.42 ± 0.10 in August. We believe this can partly be attributed to the known limitations of AMSR-E and other passive microwave sea-ice concentration retrieval algorithms during melting conditions due to varying snow properties and due to melt ponds. It is difficult to quantify the sensitivity of such algorithms to snow-property variations, because their magnitude and spatiotemporal distribution is unknown. In contrast, it should be possible to quantify the sensitivity of such algorithms to melt ponds, because these should theoretically be detected as open water. Consequently, such algorithms should provide an open-water fraction which is the sum of the fractions of leads and openings between the ice floes and of the melt ponds on the sea ice. In order to isolate the influence of the melt ponds one needs to investigate only the high ice concentration areas. The MODIS sea-ice parameter data set (sub-section 2.1), which we use, is ideal for this purpose, because it provides the open-water fraction (in leads and openings), the melt-pond fraction (on sea ice) and the net sea-ice surface fraction. By limiting our investigation to MODIS sea-ice concentrations > 90% we can take the MODIS ice-surface fraction as an inverse measure of the melt-pond fraction.

3.3 AMSR-E sea-ice concentration compared to MODIS ice-surface fraction

We compare AMSR-E sea-ice concentration (sub-section 3.2) with the MODIS ice-surface fraction (sub-section 2.1) for grid cells with MODIS sea-ice concentration > 90%. For the range of observed MODIS ice-surface fractions between about 50 and 100%, we find quite different ranges of AMSR-E sea-ice concentration (Figure 5). For the Bootstrap_f and 6H algorithm, AMSR-E sea-ice concentrations range between 80 and 150% and 75 and 125%, respectively, and suggest a relatively well-defined linear relationship (Figure 5 a,b). For July, we find a slope between AMSR-E sea-ice concentration and MODIS ice-surface fraction of 1.44 and 1.34, respectively. The respective correlation coefficients are 0.855 and 0.820. For the Bootstrap_p and NASA_Team algorithm, AMSR-E sea-ice concentrations tend to cluster in a point cloud with a shallower slope and a less well defined linear relationship (Figure 5 c,e). For July, the corresponding slopes are 1.14 and 1.23, respectively, and the respective correlation coefficients are 0.428 and 0.666. AMSR-E sea-ice concentrations derived with the ASI and the NT2 algorithm stay within 75 and 100% and within 85 and 100%, respectively

(Figure 5 d,f); the small range in AMSR-E sea-ice concentrations of these to algorithm can clearly be attributed to the cut off mentioned in the sub-section 3.2.

We obtain slope, correlation coefficient, and RMSD values of all eight algorithms (see Table 4) separately for all grid cells and only the FYI and MYI grid cells (see sub-section 2.4) and summarize these in Tables 8 to 10 for June, July, and August. For August we exclude all values obtained for FYI grid cells because of their low count of 44 (Table 10). We find an increase in the slopes from June to July for all algorithms, which is followed for July to August by a decrease for 6H, Bootstrap_f and Bristol algorithms but a further increase for Bootstrap_p and Near90_lin algorithms. Correlations between AMSR-E sea-ice concentrations and MODIS ice-surface fractions are below 0.4 in June (Table 8) – independent of using all, FYI, or MYI grid cells. In contrast, for July (Table 9) we obtain correlations > 0.8 for 6H, Bootstrap_f, and Bristol algorithms – together with the largest slopes. These suggest a considerable sensitivity of these algorithms to the melt-pond fraction. This does also apply to MYI grid cells. For July, the lowest correlation of 0.43 is obtained for the Bootstrap_p algorithm – together with the smallest slope (Table 9). This suggests the weakest sensitivity to the melt-pond fraction for the investigated algorithms.

We carried out the same inter-comparison using a MODIS sea-ice concentration threshold of 98% (not shown) instead of 90%. By using 98%, no results can be obtained for August because of too few valid data. For June and July slopes remain similar to those in Tables 8 and 9. For June, correlations are considerably smaller compared to using 90%. Correlations are a bit higher for July. Despite this better correlation in July, the peak melting period (see Figure 3), we decided to keep the 90% threshold to ensure a large enough number of data points. The results of the previous paragraph remain the same for 90% and 98% MODIS sea-ice concentration threshold.

We conclude: For one type of algorithms, AMSR-E sea-ice concentration is linearly related to the MODIS ice-surface fraction, as we hypothesized in the introduction, i.e., AMSR-E sea-ice concentrations are sensitive to the melt-pond fraction. These are the 6H, Bootstrap_f, and Bristol algorithms. For the other algorithms investigated, such a linear relationship is increasingly less pronounced in the following, descending order: NASA-Team, Near90_lin, Bootstrap_p.

4.1 Sea-ice concentration algorithm parameter space

To explain the different sensitivities to the melt pond fraction (sub-section 3.2), we start with an illustration of the distribution of AMSR-E brightness temperatures and contemporary MODIS ice-surface fraction of July 2009 in the parameter spaces of four of the algorithms (Figure 6). These algorithms are: NASA-Team, ASI or Near90_lin, as both rely on brightness temperatures near 90 GHz, and the two Bootstrap algorithms. Bootstrap_f and Bootstrap_p are the two algorithms with the highest and the lowest sensitivity of AMSR-E sea-ice concentrations to melt-pond fraction, respectively (Figure 5, Tables 8 to 10). The NASA-Team algorithm is among the most used ones and the ASI and Near90_lin algorithm have the advantage of a substantially finer grid resolution thanks to using the near 90 GHz channels. In every parameter space we show the following items:

I.   A winter-time AMSR-E brightness temperature distribution for open water (black dots) and AMSR-E NT2 sea ice concentration > 90% (white dots). The spread of the black dots results from the weather influence over open water. We refer to these as winter data points or winter brightness temperatures in the following text.

II. Winter-time open water (white cross) and sea ice (black crosses) tie points obtained from Ivanova et al. (2015) and used to compute the AMSR-E sea-ice concentration (see sub-section 2.3 for an explanation of why we use winter tie points).

III. Red arrows denote the direction of increasing sea-ice concentration.

IV. AMSR-E brightness temperatures of our data set, i.e. only for MODIS sea-ice concentration > 90% for the month of July, color coded with the contemporary MODIS ice-surface fraction. We refer to these as summer data points or summer brightness temperatures in the following text.

V.   A red line connecting FYI and MYI tie points denotes the ice line.

4.1.1 NASA-Team algorithm

For NASA-Team algorithm (Figure 6 a) summer data points from July 2009 are located well within the cloud of winter data points (see I.). The NASA-Team tie-point triangle (Cavalieri et al., 1990) is approximated by the dashed white lines and the red (ice) line (see V.). A considerable number of summer data points are located to the left of the ice line. For these data points, NASA-Team sea-ice concentrations exceed 100% and MODIS ice-surface fractions are between 80 and 100% (see the color scale). To the right of the ice line, summer

data points coincide with MODIS ice-surface fractions of ~70% and are supposed to provide NASA-Team sea-ice concentrations between 80 and 100% (compare Figure 5 c).

4.1.2 ASI or Near90_lin algorithm

For the ASI or Near90_lin algorithm (Figure 6 b) summer data points from July 2009 are also located well within the cloud of winter data points. A considerable number of the summer data points are located above the ice line (see V.). For these data points, ASI or Near90_lin sea-ice concentrations exceed 100%. Most of the summer data points located below the ice line result in ASI or Near90_lin sea-ice concentrations between 80 and 100%. The associated MODIS ice-surface fractions decrease from ~100% close to the MYI tie point to ~70% when following the summer data points towards the FYI tie point and beyond (see Figure 5 d).

4.1.3 Bootstrap_f algorithm

For the Bootstrap_f algorithm (Figure 6 c), a substantial number of summer data points from July 2009 fall outside the winter data-point cloud (see I.). The majority of the summer data points are located above the winter ice line (red: our tie points, black: Comiso et al. (1997)). The location of these data points relative to the open-water tie point, the winter ice lines and the tie points for MYI and FYI suggests, that Bootstrap_f sea-ice concentrations exceed 100% by up to a few ten percent (compare Figure 5 b). The distance between the open-water tie point and the winter ice lines increases from left (MYI tie point) to right (FYI tie point). Similar MODIS ice-surface fractions tend to intersect the winter ice lines. Therefore, the over-estimation of Bootstrap_f sea-ice concentration decreases with decreasing MODIS ice-surface fraction (see Figure 5 b).

4.1.4 Bootstrap_p algorithm

For the Bootstrap_p algorithm (Figure 6 d), only few summer data points from July 2009 are located closely above the winter ice lines (see also sub-section 4.1.3). Consequently, Bootstrap_p sea-ice concentrations do not exceed 110% (compare Figure 5 e). As for the Bootstrap_f algorithm (Figure 6 c) only very few summer data points are located close to the MYI tie point. The majority of those data points which are associated with MODIS ice-surface fractions ~70% are located in a relatively broad band parallel to the winter ice lines close to the FYI tie point. The distance between the open-water tie point and the winter ice lines increases upward along these lines. We therefore observe a wide range of Bootstrap_p

1 sea-ice concentrations between 70 and ~100% at MODIS ice-surface fractions of ~70%

2 (compare Figure 5 e).

3 4.2 Summer sea-ice tie points for the Bootstrap algorithm

4 We used open-water and sea-ice tie points representative of winter conditions (sub-section

5 2.3). We are not aware of summer sea-ice tie points for the ASI or Near90_lin and the NASA-

6 Team algorithms, but they do exist for the Bootstrap algorithm. The solid cyan line in Figure

7 6 c) denotes the summer sea-ice tie point for the Bootstrap_f algorithm taken from Comiso et

8 al. (1997). For the Bootstrap_p algorithm (Figure 6 d), the solid and dashed cyan lines denote

9 the summer sea-ice tie points for the periods July 1-18 and July 19 to August 4, respectively.

10 For the period after August 4, the summer ice line coincides with the winter ice line (black

11 line in Figure 6 d).

12 We use MODIS ice-surface fractions of the period June 20 to July 5 to derive summer tie

13 points from our summer brightness temperatures. We select only data of MODIS ice-surface

14 fractions > 97.8% and of vertically polarized 37 GHz brightness temperatures > 250 K. We

15 did not discriminate between different ice types. We compute summer sea-ice tie points

16 (Table 11) at 19, 37 and 89 GHz and from these also derive values of the normalized

17 brightness-temperature polarization difference (PR). These summer sea-ice tie points are also

18 added to Figure 6 c) and d) as cyan crosses.

19 The potential impact of using summer instead of winter sea-ice tie points will be discussed in

20 the following sub-section.

21 4.3 Temporal evolution

22 During the melting season, changes in the snow and sea-ice microphysical properties, the

23 associated variations in AMSR-E brightness temperatures, and the retrieved AMSR-E sea-ice

24 concentrations can occur within a few days. It is likely that Figures 4 to 6 do blur such

25 temporal variations which, we think, need to be discussed to understand the observed

26 differences in the sensitivity of the AMSR-E sea-ice concentration algorithms to the melt-

27 pond fraction. Therefore we sub-divide the MODIS and AMSR-E data sets used into pentads

28 (5-day periods) and discuss the temporal evolution for the four algorithms shown in Figure 6.

29 4.3.1 *NASA-Team algorithm*

30 For the NASA-Team algorithm, 1st pentad (June 1-5, Figure 7 a), most summer data points

31 are located at PR19 = ~0.03 (compare Table 11) GR3719 between -0.05 and -0.01. MODIS

32 ice-surface fractions are ~100%. About 20% of the data points belong to the MYI class while

only 7 data points belong to the FYI class (see subsection 2.4). NASA-Team sea-ice concentration and MODIS ice-surface fraction agree well with each other by means of slope and correlation coefficient. Later, summer data points cover a larger PR19 range: 0.02 to 0.08, and a larger GR3719 range: 0.0 to -0.09 (June 16-20, Figure 7 b) and: 0.0 to -0.12 (July 1-5, 6-10, Figure 7 c,d). We explain the larger PR19 range by an increase in snow density (Table 2) and snow wetness (Table 1). We explain the expansion of GR3719 towards more negative values with an increase in the surface layer snow grain size (Table 3). Figures 7 c, d) coincide with the onset of widespread melt-pond formation (see Figure 3, days 30 to 40). MODIS ice-surface fractions are still mostly > 85% in Figure 7 b), range between ~100% and ~70% in Figure 7 c) and decrease to between ~90% and 60% in Figure 7 d). With further melt progress, the PR19-GR3719 cloud shrinks to GR3719 values of +0.01 to -0.06 on July 21-25 (Figure 6 f). At this stage MODIS ice-surface fractions are between 60% and 80%.

NASA-Team sea-ice concentrations exceed 100% on June 16-20 and especially July 1-5 (Figures 7 b,c) with values up to 120%. We find only few values > 100% for July 21-25, shortly after peak melt (Figure 7 f). After the good agreement between NASA-Team sea-ice concentration and MODIS ice-surface fraction for June 1-5 (Figure 7 a) it breaks down. During July the correlation between NASA-Team sea-ice concentration and MODIS ice-surface fraction increases again, together with the slope, which reaches 1.31 for the pentad July 21-25 (Figure 7 f, compare Table 9). Correlations are ~0.5 for most of July which corresponds to an explained variance of about 25%. Therefore, after the onset of wide-spread melt-pond formation beginning of July 2009, NASA-Team sea-ice concentrations and MODIS ice-surface fractions are linearly related to some degree, i.e. the NASA-Team algorithm is sensitive to melt ponds. The relatively low correlation highlights the importance of other processes such as changes in those snow and sea-ice properties, which influence GR3719. These can be snow grain size and wetness (Tables 1 and 3) and, after snow melt, sea-ice salinity, roughness, and density [Eppler et al., 1992; Hallikainen and Winebrenner, 1992].

4.3.2 *Bootstrap_f algorithm*

For the Bootstrap_f algorithm, 1st pentad (June 1-5, Figure 8 a), most summer data points are associated with MODIS ice-surface fractions ~100%, are located beyond the upper border of the winter data points and above the winter ice line (see Figure 6 c). Most Bootstrap_f sea-ice concentrations exceed 100% and the MODIS ice-surface fraction is over-estimated. We can

attribute these elevated brightness temperatures to elevated snow wetness (and density) which causes a larger increase in the vertically polarized brightness temperatures at 37 GHz than at 19 GHz (Table 1). On June 16-20 (Figure 8 b), almost all summer data points are located above the winter ice line and almost all Bootstrap_f sea-ice concentrations are > 100%,; maxima exceed 140%. The cluster of MODIS ice-surface fractions of ~95% coincides with the cluster of Bootstrap_f sea-ice concentrations centred at 130%. Until July 1-5 (Figure 8 c), the summer data points cloud gradually expands towards lower values. Associated MODIS ice-surface fractions are lowest (~70%) along the bottom of the cloud and highest (~95%) at its left end. We attribute the latter to melt-refreeze cycles causing an increase in snow grain size associated with a smaller brightness-temperature decrease at 19 GHz than at 37 GHz (Table 3). These grid cells at the left end of the cloud are responsible for Bootstrap_f sea ice concentrations of ~140% (compare Figure 8 c) and 6 c). Throughout the remaining three pentads (Figure 8 d) to f), summer data points are shifted towards lower 19 GHz brightness temperatures and are covering a smaller range at both frequencies. We attribute this to complete snow melt. Snow wetness and grain size variations do not influence the brightness temperatures anymore MODIS ice-surface fractions are between 60 and 80% now (Figure 8 f), compare Figure 7 f). Maximum Bootstrap_f sea-ice concentrations have decreased to ~120% until July 21-25.

The good agreement between Bootstrap_f sea-ice concentration and MODIS ice-surface fraction in the 1st June pentad breaks down during June and re-emerges during July. Between the 3rd July and the 2nd August pentad average correlations are ~0.65 explaining > 40% of the variance. The average slope is 1.45 for these 6 pentads. Therefore, with the onset of wide-spread melt-pond formation also Bootstrap_f sea-ice concentrations and MODIS ice-surface fractions are linearly related to each other, i.e., the Bootstrap_f algorithm is sensitive to melt ponds. This sensitivity is stronger than for the NASA-Team algorithm (sub-section 4.3.1) which could be explained by a smaller influence of the other surface properties mentioned above in the previous sub-section.

It is difficult to quantify how this result would change by using summer sea-ice tie points, which we did not use to compute AMSR-E sea-ice concentrations with the two Bootstrap algorithms for the reasons given in sub-section 2.3, but did include in Figure 6 c,d) as cyan lines. The distance between the cyan line and the winter ice lines in proximity to the FYI tie point, measured along the dashed white line, suggests that we would reduce Bootstrap_f sea-

ice concentrations by 10% to 15%. Therefore, at this side of the parameter space, Bootstrap_f sea-ice concentrations would be ~100%. However, to the left of the FYI tie point the location of the summer data points (Figure 6c), Figure 8 c,d) suggests, that Bootstrap_f sea-ice concentrations would still be > 120%. Therefore, using summer sea-ice tie points would reduce the slope between Bootstrap_f sea-ice concentrations and MODIS ice-surface fractions but whether the correlations would be similarly high and whether we can exclude unknown non-linear effects cannot be answered in the present paper.

4.3.3   *The other algorithms*

The temporal evolution of Bootstrap_p sea-ice concentrations in relation to the MODIS ice-surface fraction during June is similar to the Bootstrap_f algorithm (Supplementary Figure S1 a,b). One principal difference is the smaller slope we obtain with Bootstrap_p sea-ice concentrations compared to the Bootstrap_f algorithm: ~0.9 vs. ~1.1 for June 1-5 and ~1.1 vs. 1.3 for July 1-5; also correlations are smaller. Secondly, we find larger variations of Bootstrap_p sea-ice concentrations around MODIS ice-surface fractions, for example 50% to 110% at 90% ice surface fraction. We attribute this to the large and polarization dependent sensitivity of 37 GHz brightness temperatures to variations in snow properties (Tables 1 to 3). In June, any linear relationship to the emerging melt-pond coverage is obscured by this sensitivity. During the first two July pentads, scatter is as high as during most of June. Brightness temperatures associated with MODIS ice-surface fractions of ~90% and ~60% are often located right next to each other in the algorithms' parameter space (Supplementary Figure S1 c,d) which is different to the Bootstrap_f algorithm (Figure 8 c,d). After mid-July, a linear relationship between Bootstrap_p sea-ice concentration and MODIS ice-surface fraction emerges. The average slope is 1.25 and correlations increase from 0.34 (July 16-20) to 0.76 (August 6-10). In summary, also the Bootstrap_p algorithm is sensitive to melt-ponds. The sensitivity is smaller than for the Bootstrap_f algorithm and snow property variations seem to be of larger influence.

How does this results change if we use summer sea-ice tie points (Figure 6 d), cyan lines) and sub-section 4.3.2)? The early summer ice line (Figure 6 d), solid cyan line) is steeper than the winter ice lines and intersects these close to the FYI tie point. Therefore, close to the FYI tie point and to the right, all summer data points are below the summer ice line causing Bootstrap_p sea-ice concentrations < 100%. However, to the left of the FYI tie point, summer data points are located above the summer ice line causing Bootstrap_p sea-ice concentrations

of up to ~130% close to the MYI tie point. Therefore, for data from 2009, using the early summer sea-ice tie points would not generally provide sea-ice concentrations, which improve the relationship between Bootstrap_p sea-ice concentrations and MODIS ice-surface fractions. The mid-summer ice line (Figure 6 d), dashed cyan line) is located parallel below the winter ice lines. A large fraction of the summer data points is located above the summer ice line causing Bootstrap_p sea-ice concentrations > 100%. For instance, for July 21-25 (Supplementary Figure S1 f), about 1/3 of the data points would have a Bootstrap_p sea-ice concentration > 100%; currently: 3 data points. Therefore, for data from 2009, using the mid-summer sea-ice tie points would increase Bootstrap_p sea-ice concentrations increasing the slope between these and MODIS ice-surface fractions, but would not necessarily improve the correlation. Compared to the winter sea-ice tie points, using the early-summer (mid-summer) sea-ice tie points would result in a decreased (enhanced) sensitivity of the Bootstrap_p algorithm to melt ponds.

The temporal development of brightness temperatures, sea-ice concentrations and ice-surface fractions obtained with the Near90_lin algorithm (Supplementary Figure S2, Figure 6 b) is comparable to that obtained with the Bootstrap_p algorithm (Supplementary Figure S1). The scatter in summer data points and between Near90_lin sea-ice concentrations and MODIS ice-surface fractions is a little less pronounced and peaks earlier. We attribute the scatter again to snow property variations (Table 1-3). For the smaller electromagnetic wavelength at 89 GHz compared to 37 GHz scattering by coarse-grained snow is more effective than the impact of snow wetness which is evident in the migration of summer data points towards lower values (compare Supplementary Figures S1 b) and S2 b). Maximum Near90_lin sea-ice concentrations of ~ 120% (Supplementary Figure S2 b) are larger than we expect from comparison with Figure 6 b) and can possibly be attributed to an unaccounted weather influence in the open-water tie point (Figure 6b), white line). After mid-July, correlations increase to their maximum in August 6-10 of 0.81. Slopes are considerably larger than for the Bootstrap_p sea-ice concentration and vary around 1.33. Both, slopes and correlations vary considerably between pentads which we attribute mainly to the larger weather influence at 89GHz. Enhanced sensitivity of surface property variations, be it remaining or new snow (Grenfell, 1986) or sea-ice surface wetness changes, at the smaller electromagnetic wavelength at 89 GHz might also contribute. We conclude that the Near90_lin algorithm or other algorithms employing near-90 GHz data such as the ASI algorithm, is sensitive to melt ponds only to some degree. Snow and sea-ice property variations but also the weather

1   influence impact sea-ice concentration retrieval with this type of algorithm as much as / more

2   than obtained for the Bootstrap_p algorithm.

3   With respect to the 6H algorithm and the Bristol algorithm we state, that both algorithms

4   reveal a temporal development of slopes and correlations between AMSR-E sea-ice

5   concentrations and MODIS ice-surface fractions (Supplementary Figures S3 and S4, Tables

6   8-10), which are similar to the Bootstrap_f algorithm. Both algorithms, 6H more than Bristol,

7   are sensitive to melt ponds.

4.3.4   *Implications for summer sea-ice concentrations*

9   A MODIS ice-surface fraction value of 60% can in reality be anything between A) 100% sea

10   ice with 40% melt-pond fraction and B) 60% sea ice with 0% melt-pond fraction. Slopes

11   between the AMSR-E sea-ice concentration and the MODIS ice-surface fraction obtained, for

12   example, for the NASA-Team algorithm, of 1.31 (Figure 7 f) would convert 60% MODIS ice-

13   surface fraction into 78% NASA-Team sea-ice concentration. In case B) this would be an

14   *over-estimation* by 18%, while in case A) this would be an *under-estimation* by 22%.

15   We compute the average slope and correlation values of all algorithms, except ASI and NT2,

16   for the 6 pentads July 11-15 to August 6-10 together with resulting over- or under-estimation

17   of case A and case B actual sea-ice concentrations for which we chose ice-surface fractions of

18   60% and 80%. The Bootstrap_f algorithm is most sensitive to melt ponds (highest slope),

19   followed by the Bristol and 6H algorithms (Table 12). The Bootstrap_p algorithm is least

20   sensitive to melt ponds (lowest slope), followed by the NASA-Team algorithm. This

21   sensitivity is most pronounced for the Bristol algorithm (largest correlation), followed by the

22   Bootstrap_f algorithm. The sensitivity is least pronounced for the Near90_lin algorithm

23   (smallest correlation), followed by the Bootstrap_p algorithm. Most pronounced means that

24   snow and sea-ice property variations as well as the weather influence have a comparably

25   small influence. These variations have a larger influence on AMSR-E sea-ice concentrations

26   retrieved with an algorithm with a less pronounced sensitivity to melt ponds. The algorithms

27   with the largest sensitivity to melt-ponds interestingly provide the smallest *under-estimation*

28   of the concentration of melt-pond covered sea ice and the largest *over-estimation* of the

29   concentration of non-ponded sea ice (e.g. the Bootstrap_f and Bristol algorithms, Table 12).

30   The algorithms with the smallest sensitivity to melt ponds provide the largest *under-*

1 *estimation* of the concentration of melt-pond covered sea ice and the smallest *over-estimation*

2 of the concentration of non-ponded sea ice (e.g. Bootstrap_p, Table 12).

3 Using summer sea-ice tie points for the Bootstrap_f algorithm would presumably reduce the

4 mean slope as discussed in sub-section 4.3.2, leading to smaller under- and over-estimation of

5 case A and case B sea-ice concentrations compared to Table 12. Using the mid-summer tie

6 point for the Bootstrap_p algorithm would, in the contrary, presumably increase the mean

7 slope as discussed in section 4.3.3, leading to a larger under- and over-estimation of case A

8 and B sea-ice concentrations compared to Table 12.

9 We investigate the sensitivity to melt ponds of eight sea-ice concentration retrieval algorithms

10 based on satellite microwave brightness temperatures by comparing contemporary daily

11 estimates of sea-ice concentration and melt-pond fraction. We derive gridded daily sea-ice

12 concentrations from Advanced Microwave Scanning Radiometer aboard Earth Observation

13 Satellite (AMSR-E) brightness temperatures of June to August 2009. We use a consistent set

14 of tie points to aid inter-comparison of the algorithms. We derive gridded daily fraction of

15 melt-ponds, open water between ice floes and ice-surface fraction from contemporary

16 Moderate Resolution Spectroradiometer (MODIS) reflectance measurements with a neural

17 network based classification approach. We discuss potential uncertainty sources of this data

18 and conclude that MODIS ice-surface fractions are as accurate as 5-10%. We carry out the

19 comparison of AMSR-E and MODIS data sets at 100 km grid resolution.

20 AMSR-E sea-ice concentrations agree fairly well with MODIS sea-ice concentrations, the

21 sum of the ice-surface fraction and the melt-pond fraction, with slopes of a linear regression

22 between 0.90 and 1.16. However, for some algorithms AMSR-E sea-ice concentrations scatter

23 widely for MODIS sea-ice concentrations larger than 80%. We note that the eventual

24 overestimation of the concentration of the sea ice in between the melt ponds, to produce

25 seemingly 'correct' sea-ice concentrations that include the melt ponds, will result in

26 incorrectly overestimating the concentration of sea ice in areas with real open water.

27 We isolate the influence of melt ponds by comparing AMSR-E sea-ice concentrations with

28 MODIS ice-surface fractions only for grid cells with MODIS sea-ice concentrations above

29 90%. By doing so we can use the ice-surface instead of the melt-pond fraction as a measure of

30 the impact of melt ponds and can keep the effect of potential misclassification between the

31 two spectrally close surface types, open water and melt ponds, as small as possible. For most

32 of June, we find a non-linear relation between both data sets. We attribute this to the influence

of snow-property variations impacting the microwave brightness temperatures and a still small melt-pond fraction. After June, for one group of algorithms, e.g., the Bristol and Comiso Bootstrap frequency mode (Bootstrap_f) algorithms, sea-ice concentrations are linearly related to MODIS ice-surface fractions. For other algorithms, e.g., Near90GHz and Comiso Bootstrap polarization mode (Bootstrap_p), the linear relationship is weaker and develops later in summer.

We take the degree of correlation between AMSR-E sea-ice concentration and MODIS ice-surface fraction as a measure of how sensitive a respective algorithm to the melt ponds is and use the obtained linear regression slope to estimate differences between actual and retrieved sea-ice concentration. All algorithms *under-estimate* the sea-ice concentration of 100% sea ice with an open-water fraction of 40% due to melt ponds (case A) by between 14% (Bootstrap_f) and 26% (Bootstrap_p). The under-estimation reduces to 0% for a melt-pond fraction of ~20%. The concentration of sea ice with a similarly large open-water fraction due to leads and openings between the ice floes (case B) is *over-estimated* by between 14% (Bootstrap_f) and 26% (Bootstrap_p) for 60% sea-ice concentration and by 20% for all algorithms for 80% sea-ice concentration.

One next step would be to extend the analysis to more years to confirm the results of our case study with a larger number of data. Currently, at pentad scale, the number of data is too small to use – as an important next step – a higher MODIS sea-ice concentration threshold of 98% instead of 90% to isolate the influence of melt ponds. At monthly scale, e.g. for July, the correlation between AMSR-E sea-ice concentrations and MODIS ice-surface fraction increases from 0.86 to 0.92 (Bootstrap_f), from 0.85 to 0.91 (Bristol), and from 0.67 to 0.76 (NASA-Team) while the slopes of the linear regression remain similar.

For reasons outlined in the description of the algorithms we use a consistent set of sea-ice tie points derived for winter conditions. By applying published summer sea-ice tie points for the Bootstrap algorithms we find that the slopes of the linear regression would be reduced for Bootstrap_f but not for Bootstrap_p. As a result Bootstrap_f would under-estimate sea-ice concentrations for case A less but over-estimate sea-ice concentrations for case B more.

We suggest, that algorithms being more sensitive to melt ponds, could be easier optimized further, because the influence of snow and sea-ice surface property variations, which distribution is unknown, seems to be less pronounced while methods to derive melt-pond fraction, which would be needed for the optimization, have been developed. According to our results, this applies to the Bootstrap_f, Bristol, and Near90_lin algorithms. The Bootstrap_p

and NASA-Team algorithms seem to be less suitable for further optimization. While these seem to have the lowest sensitivity to melt ponds and therefore lowest under-estimation for case A, they seem to over-estimate the sea-ice concentration for case B most, among the algorithms investigated.

Acknowledgements

We thank the data providers: NASA DAAC for AMSR-E L2 brightness temperatures and MODIS L1B reflectance data, NSIDC for AMSR-E L3 sea ice concentrations. Sea ice age data are originally provided by Mark Tschudi, CCAR, University of Colorado, Boulder, CO, and were obtained in netCDF format from the Integrated Climate Data Center (ICDC, http://icdc.zmaw.de) University of Hamburg, Hamburg, Germany for the year 2009. This work was funded by ESA/ESRIN (sea ice CCI). S. Kern acknowledges support from the Center of Excellence for Climate System Analysis and Prediction (CliSAP), University of Hamburg, Germany; A. Rösel acknowledges support from TO BE INCLUDED.

NT2 SIC is taken from the AMSR-E/Aqua Daily L3 12.5 km Brightness Temperature, Sea Ice Concentration, & Snow Depth Polar Grids product (http://nsidc.org/data/docs/daac/ae_si12_12km_tb_sea_ice_and_snow.gd.html, (Cavalieri et al., 2014)) available from NSIDC.

References

Andersen, S., Tonboe, R. T., Kaleschke, L., Heygster, G., and Pedersen, L. T.: Intercomparison of passive microwave sea ice concentration retrievals over the high-concentration Arctic sea ice, J. Geophys. Res., 112, C08004, 2007.

Ashcroft, P. and Wentz, F. J.: AMSR-E/Aqua L2A Global Swath Spatially-Resampled Brightness Temperatures. Version 3. (2009-06-01 to 2009-08-31). Boulder, Colorado USA: NASA DAAC at the National Snow and Ice Data Center. http://dx.doi.org/10.5067/AMSR-E/AE_L2A.003, 2013.

Baum, B. A., Menzel, W. P., Frey, R. A., Tobin, D. C., Holz, R. E., and Ackerman, S. A.: MODIS cloud-top property refinement for Collection 6, J. Appl. Meteorol. Climatol., 51(6), 1145-1163, 2012, doi:1175/JAMC-D-11-0203.1.

Beitsch, A. Uncertainties of a near 90 GHz sea ice concentration retrieval algorithm. Dissertationsschrift, Universität Hamburg, 2014. URL: http://ediss.sub.uni-hamburg.de/volltexte/2014/7070/pdf/Dissertation.pdf (Stand: 2.06.2016).

Cavalieri, D. J., Markus, T., and Comiso, J. C.: AMSR-E/Aqua Daily L3 12.5 km Brightness Temperature, Sea Ice Concentration, & Snow Depth Polar Grids. Version 3. (June-August 2009). Boulder, Colorado USA: NASA National Snow and Ice Data Center Distributed Active Archive Center. doi: 10.5067/AMSR-E/AE_SI12.003, 2014.

Cavalieri, D. J., Burns, B. A., and Onstott, R. G.: Investigation of the effects of summer let on the calculation of sea ice concentration using active and passive microwave data, J. Geophys. Res., 95(C4), 5359-5369, 1990.

Cavalieri, D. J., Gloersen, P., and Campbell, W. J.: Determination of sea ice parameters with the NIMBUS 7 SMMR, J. Geophys. Res., 89(D4), 5355–5369, 1984.

Chan, M. A. and Comiso, J. C.: Arctic cloud characteristics as derived from MODIS, CALIPSO, and CloudSat, J. Clim., 26(10), 3285-3306, doi:10.1175/JCLI-D-12-00204.1, 2013.

Comiso, J. C.: Large decadal decline of the Arctic multiyear ice cover, J. Clim., 25(4), 1176-1193, 2012, doi:10.1175/JCLI-D-11-00113.1.

Comiso, J. C.: Enhanced sea ice concentrations and ice extents from AMSR-E data, J. Rem. Sens. Soc. Japan, 29(1), 199-215, 2009.

Comiso, J. C.: Characteristics of arctic winter sea ice from satellite multispectral microwave observations, J. Geophys. Res., 91(C1), 975–994, 1986.

Comiso, J. C. and Kwok, R.: Surface and radiative characteristics of the summer Arctic sea ice cover from multisensory satellite observation, J. Geophys. Res., 101(C12), 28,397-28,416, 1996.

Comiso, J. C., Cavalieri, D. J., Parkinson, C. L., and Gloersen, P.: Passive microwave algorithms for sea ice concentration: A comparison of two techniques, Rem. Sens. Environ., 60(3), 357-384, 1997.

Divine, D. V., Granskog, M. A., Hudson, S. R., Pedersen, C. A., Karlsen, T. I., Divina, S. A., Renner, A. H. H., and Gerland, S.: Regional melt-pond fraction and albedo of thin Arctic first-year drift ice in late summer, The Cryosphere, 9(1), 225-268, 2015, doi:10.5194/tv-9-255-2015.

Eastwood, S. (Ed.): Ocean & Sea Ice SAF (OSISAF) Sea Ice Product Manual. Version 3.8., http://osisaf.met.no, May 2012.

Eicken, H., Grenfell, T. C., Perovich, D. K., Richter-Menge, J. A., and Frey, K.: Hydraulic controls of summer Arctic pack ice albedo, J. Geophys. Res., 109, C08007, doi:10.1029/2003JC001989, 2004.

Eppler, D. T., Farmer, L. D., Lohanick, A. W., Anderson, M. R., Cavalieri, D. J., Comiso, J. C., Gloersen, P., Garrity, C., Grenfell, T. C., Hallikainen, M., Maslanik, J. A., Mätzler, C., Melloh, R. A., Rubinstein, I., and Swift, C. T.: Passive microwave signatures of sea ice, in Carsey, F.: Microwave remote sensing of sea ice, AGU Monograph 68, pp. 47-71, 1992.

Fetterer, F., and Untersteiner, N.: Observations of melt ponds on Arctic sea ice, J. Geophys. Res., 103(C11), 24821-24835, 1998.

Flocco, D., Feltham, D. L., and Turner, A. K.: Incorporation of a physically based melt pond scheme into the sea ice component of a climate model, J. Geophys. Res., 115, C08012, doi:10.1029/2009JC005568, 2010.

Fowler, C., Emery, W., and Maslanik, J. A.: Satellite derived arctic sea ice evolution Oct. 1978 to March 2003, Trans. Geosci. Rem. Sens. Lett., 1(2), 71‑74, 2003.

Fuhrhop, R., Grenfell, T. C., Heygster, G., Johnsen, K,-P., Schlüssel, P., Schrader, M., and Simmer, C.: A combined radiative transfer model for sea ice, open ocean, and atmosphere, Radio Sci., 33(2), 303-316, 1998.

Garrity, C.: Characterization of snow on floating ice and case studies of brightness temperature changes during the onset of melt, in Carsey, F.: Microwave remote sensing of sea ice, AGU Monograph 68, pp. 313-328, 1992.

1 Gogineni, S. P., Moore, R. K., Grenfell, T. C., Barber, D. G., Digby, S., and Drinkwater, M.:
2 The effects of freeze-up and melt process on microwave signature, in Carsey, F.: Microwave
3 remote sensing of sea ice, AGU Monograph 68, chapter 17, 1992.

4 Grenfell, T. C., and Lohanick, A. W.: Temporal variations of the microwave signature of sea
5 ice during the late spring and early summer near Mould Bay, Northwest Territories, J.
6 Geophys. Res., 90(C3), 5063-5074, 1985.

7 Hallikainen, M., and Weinbrenner, D. P.: The physical basis for sea ice remote sensing, in
8 Carsey, F.: Microwave remote sensing of sea ice, AGU Monograph 68, chapter 3, pp.47-71,
9 1992.

10 Holland, M. M., Bailey, D. A., Briegleb, B. P., Light, B., and Hunke, E.: Improved sea ice
11 shortwave radiation physics in CCSM4: The impact of melt ponds and aerosols on Arctic sea
12 ice, J. Clim., 25(5), 1413-1430, doi:10.1175/JCLI-D-11-00078.1, 2012.

13 Istomina,L., Heygster, G., Huntemann, M., Schwarz, P., Birnbaum, G., Scharien, R.,
14 Polashenski, C., Perovich, D., Zege, E., Malinka, A., Prikhach, A., and Katsev, I.: Melt pond
15 fraction and spectral sea ice albedo retrieval from MERIS data − Part 1: Validation against in
16 situ, aerial, and ship cruise data, The Cryosphere, 9, 1551-1566, doi:10.5194/tc-9-1551-2015,
17 2015.

18 Istomina, L., Heygster, G., Huntemann, M., Marks, H., Melsheimer, C., Zege, E., Malinka,
19 A., Prikhach, A., and Katsev, I.: Melt pond fraction and spectral sea ice albedo retrieval from
20 MERIS data − Part 2: Case studies and trends of sea ice albedo and melt ponds in the Arctic
21 for years 2002–2011, The Cryosphere, 9, 1567-1578, doi:10.5194/tc-9-1567-2015, 2015.

22 Ivanova, N., Pedersen, L. T., Tonboe, R. T., Kern, S., Heygster, G., Lavergne, T., Sorensen,
23 A., Saldo, R., Dybkjaer, G., Brucker, L., and Shokr, M.: Satellite passive microwave
24 measurements of sea ice concentration: an optimal algorithm and challenges, The Cryosphere,
25 9, 1797-1817, doi:10.5194/tc-9-1797-2015, 2015.

26 Ivanova, N., L. T. Pedersen, and R. T. Tonboe, Product Validation and Algorithm Selection
27 Report (PVASR): Sea Ice Concentration, version 1.1, 28 August 2013, SICCI Project Report
28 D2.5, Doc Ref: SICCI-PVASR (SIC), 2013.

29 Ivanova, N., Pedersen, L. T., Lavergne, T., Tonboe, R. T., Rinne, E., and Ridout, A.:
30 Algorithm Theoretical Basis Document, version 1.0 (ATBDv2), May 13, SICCI Project
31 Report D3.6, Doc Ref: SICCI-ATBDv2-13-09, 2014.

Kaleschke L., Lüpkes, C., Vihma, T., Haarpaintner, J., Bochert, A., Hartmann, J., and Heygster, G.: SSM/I Sea Ice Remote Sensing for Mesoscale Ocean-Atmosphere Interaction Analysis, Can. J. Remote Sens., 27, 5, 526–537, 2001.

Karlsson, K. G. and Dybbroe, A.: Evaluation of Arctic cloud products from the EUMETSAT Climate Monitoring Satellite Application Facility based on CALIPSO–CALIOP observations. Atmos. Chem. Phys., 10, 1789-1807, 2010.

Kern, S., Zygmuntowska, Khvorostovsky, K. Spreen, G., Ivanova, N. and Beitsch, A.: Product Validation and Intercomparison Report, PVIR, Version 1.1, 25. Feb. 2015, SICCI Project Report D4.1, Doc Ref: SICCI-PVIR.

King, M. D., Platnick, S., Menzel, W. P., Ackerman, S. A., and Hubanks, P. A.: Spatial and temporal distribution of clouds observed by MODIS onboard the Terra and Aqua Satellites, IEEE Trans. Geosci. Rem. Sens., 51(7), 3826-3852., 2013

Landy, J., Ehn, J., Shields, M., and Barber, D.: Surface and melt pond evolution on landfast first-year sea ice in the Canadian Arctic Archipelago, J. Geophys. Res. - Oceans, 119, 3054-3075, doi:10.1002/2013JC009617, 2014.

Mäkynen, M., Kern, S., Rösel, A., and Pedersen, L. T.: On the estimation of melt pond fraction on the Arctic sea ice with Envisat WSM images, Trans. Geosci. Rem. Sens., 52(11), doi:10.1109/TGRS.2014.2311476, 2014.

Markus, T. and Cavalieri, D. J.: An enhancement of the NASA Team sea ice algorithm, Trans. Geosci. Rem. Sens., 38(3), 1387–1398, 2000.

Markus, T., Cavalieri, D. J., Tschudi, M. A., and Ivanoff, A.: Comparison of aerial video and Landsat 7 data over ponded sea ice, Rem. Sens. Environ., 86, 458-469, 2003.

Maslanik, J., Stroeve, J., Fowler, C., and Emery, W.: Distribution and trends in Arctic sea ice age through spring 2011, Geophys. Res. Lett., 38, L13502, doi:10.1029/2011GL047735, 2011.

Maykut, G. A., and Untersteiner, N.: Some results from a time dependent thermodynamic model of Arctic sea ice, J. Geophys. Res., 76, 1550-1575, 1971.

Meier, W.: Comparison of passive microwave ice concentration algorithm retrievals with AVHRR imagery in the Arctic peripheral seas, Trans. Geosci. Rem. Sens., 43(6), 1324-1337, doi: 10.1109/TGRS.2005.846151, 2005.

Pedersen, L.T.: Merging microwave radiometer data and meteorological data for improved sea ice concentrations, EARSeL Advances in Remote Sensing, Vol. 3, No. 2-XII, 1994.

Perovich, D. K., Richter-Menge, J., Polashenski, C., Elder, B., Arbetter, T., and Brennick, G.: Sea ice mass balance observations from the North Pole Environmental Observatory, Geophys. Res. Lett., 41(6), 2019-2025, doi:10.1002/2014GL059356, 2014.

Perovich, D. K., Tucker III, W. B., and Ligett, K. A.: Aerial observations of the evolution of ice surface conditions during summer, J. Geophys. Res., 107(C10), 8048, doi:10.1029/2000JC000449, 2002.

Perovich, D. K. and Polashenski, C.: Albedo evolution of seasonal Arctic sea ice, Geophys. Res. Lett., 39, L08501, doi:10.1029/2012GL051432, 2012.

Petrich, C., Eicken, E., Polashenski, C. M., Sturm, M., Harbeck, J. P., Perovich, D. K., and Finnegan, D. C.: Snow dunes: A controlling factor of melt pond distribution on Arctic sea ice, J. Geophys. Res., 117, C09029, doi:10.1029/2012JC008192, 2012.

Polashenski, C., Perovich, D. K., and Courville, Z.: The mechanisms of sea ice melt pond formation and evolution, J. Geophys. Res., 117, C01001, doi:10.1029/2011JC007231, 2012.

Rösel, A., Kaleschke, L., and Birnbaum, G.: Melt ponds on Arctic sea ice determined from MODIS satellite data using an artificial neural network, The Cryosphere, 6, 431-446, 2012a.

Rösel, A., Kaleschke, L., and Kern, S.: Influence of melt ponds on microwave sensor's sea ice concentration retrieval algorithms, IGARSS 2012, Munich, Germany, July 23-27, 2012b.

Sankelo, P., Haapala, J., Heiler, I., and Rinne, E.: Melt pond formation and temporal evolution at the drifting station Tara during summer 2007, Polar Res., 29(3), doi:10.1111/j.1751-8369.2010.00161.x.

Smith, D. M.: Extraction of winter total sea-ice concentration in the Greenland and Barents Seas from SSM/I data, Int. J. Rem. Sens., 17, 13, 2625–2646, 1996.

Spreen, G., Kaleschke, L., and Heygster, G.: Sea ice remote sensing using AMSR-E 89-GHz channels, J. Geophys. Res., 113, C02S03, doi:10.1029/2005JC003384, 2008.

Steffen, K. and Schweiger, A.: NASA team algorithm for sea ice concentration retrieval from Defense Meteorological Satellite Program special sensor microwave imager: comparison with Landsat satellite data, J. Geophys. Res., 96(C12), 21,971-21,987, 1991.

Stiles, W. H. and Ulaby, F. T.: The active and passive microwave response to snow parameters: 1. Wetness, J. Geophys. Res., 85(C2), 1037-1044, doi.10.1029/JC085iC02p01037, 1980.

Swan, A. M., and Long, D. G.: Multiyear Arctic sea ice classification using QuikSCAT, IEEE Trans. Geosci. Rem. Sens., 50(9), 2012, doi:10.1109/TGRS.2012.2184123.

1   Tschudi, M., C. Fowler, J. Maslanik, J. S. Stewart, and W. Meier. 2016. EASE-Grid Sea Ice

2   Age, [indicate subset used]. Boulder, Colorado USA: NASA National Snow and Ice Data

3   Center Distributed Active Archive Center. http://dx.doi.org/10.5067/PFSVFZA9Y85G.

4   Tschudi, M., Fowler, C., Maslanik, J., and Stroeve, J.:. Tracking the movement and changing

5   surface characteristics of Arctic sea ice, IEEE J. Selec. Top. Appl. Earth Obs. Rem. Sens.,

6   3(4), 536-540, 2010.

7   Tschudi, M. A., Maslanik, J. A., and Perovich, D. K.: Derivation of melt pond coverage on

8   Arctic sea ice using MODIS observations, Rem. Sens. Environ., 112, 2605-2614, 2008.

9   Tschudi, M. A., Curry, J. A., and Maslanik, J. A.: Airborne observations of summertime

10   surface features and their effect on surface albedo during FIRE/SHEBA, J. Geophys. Res.,

11   106(D14), 15,335-15,344, 2001.

12   Ulaby, F. T., Moore, R. K., and Fung, A. K.: Microwave remote sensing, active and passive.

13   Volume III: From theory to applications, Addison Wesley Pub. London, U.K., 1986.

14   Warren, S. G., Rigor, I. G., Untersteiner, N., Radionov, V. F., Bryazgin, N. N., Aleksandrov,

15   Y. I., and Colony, R.: Snow depth on Arctic sea ice. J. Clim., 12, 1814-1829, 1999.

16   Webster, M. A., Rigor, I. G., Perovich, D. K., Richter-Menge, J. A., Polashenski, C. M., and

17   Light, B.: Seasonal evolution of melt ponds on Arctic sea ice. J. Geophys. Res. – Oceans,

18   120(9), 5968-5980, 2015, doi:10.1002/2015JC011030.

19   Willmes, S., Nicolaus, M., and Haas, C.: The microwave emissivity variability of snow

20   covered first-year sea ice from late winter to early summer: a model study, The Cryosphere, 8,

21   891-904, doi:10.5194/tc-8-891, 2014.

22   Yackel, J. J. and Barber, D. G.: Melt ponds on sea ice in the Canadian Archipelago: 2. On the

23   use of RADARSAT-1 synthetic aperture radar for geophysical inversion, J. Geophys. Res.,

24   105(C9), 22,061-22,070, 2000.

25   Zege, E., Malinka, A., Katsev, I., Prikhach, A., Heygster G., Istomina, L., Birnbaum, G., and

26   Schwarz, P.: Algorithm to retrieve the melt pond fraction and the spectral albedo of Arctic

27   summer ice from the satellite optical data, Rem. Sens. Environ., 163, 153-164,

28   doi:10.1016/j.rse.2015.03.012, 2015.

Table 1: Typical values of changes in brightness temperature due to changes in snow wetness. Abbreviations TB, PR, GR, V, and H denote brightness temperature, normalized brightness temperature polarization difference ("polarization ratio"), normalized brightness temperature frequency difference ("gradient ratio"), vertical, and horizontal (polarization), respectively. Abbreviations E92, W14, and G92 refer to Eppler et al. (1992), Willmes et al. (2014), and Garrity (1992), respectively.

Snow wetness	E92	W14	W14	G92
Change by	Typical May to June increase (~ 2%)	Average May to June increase	Melt after refreeze	+ 2%
TB19H	+25 K	+16 K	+5 K	
TB19V	+20 K	+14 K	+7 K	
TB37H	+40 K	+32 K	+25 K	+34K
TB37V	+30 K	+32 K	+10 K	+15K
TB89H		+50 K		
TB89V		+60 K		
PR19			+0.02	
GR3719			+0.05	

1   Table 2: Typical values of changes in brightness temperature due to changes in snow density.

2   For abbreviations TB, PR, GR, V, and H see Table 1. Abbreviations F98 and B15 refer to

3   Fuhrhop et al. (1998) and Beitsch (2014), respectively.

Snow density	F98	B15
Change by	+200 kg/m³	+50 kg/m³
PR19	+0.04	
GR3719	0.00	
TB89V-TB89H		+2.5 K

1   Table 3: Typical values of changes in brightness temperature due to changes in snow grain

2   size. For abbreviations TB, PR, GR, V, and H see Table 1. Abbreviations F98, W14, and G92

3   refer to Fuhrhop et al. (1998), Willmes et al. (2014), and Garrity (1992), respectively.

Snow grain size	F98	F98	W14	G92
	Upper snow layer	Bottom snow layer	Upper snow layer	
Change by	+0.5mm	+0.5mm	Increase due to surface refreezing	Increase due to surface crust formation
GR3719	-0.025	+0.05	-0.04	
PR19	+0.01	+0.02	0.0	
TB37V			-20K	-10K
TB37H			-35K	-20K
TB19V			-10K	
TB19H			-15K	

1   Table 4. The sea ice concentration algorithms. *Analysis not shown in this study.

Algorithm	Acronym	Reference	Frequencies/Combination
Bootstrap_p	BP	Comiso, 1986	37V, 37H
Bootstrap_f/ CalVal	BF	Comiso, 1986	19V, 37V
Bristol	BR	Smith, 1996	19V, 37V, 37H
NASA Team	NT	Cavalieri et al., 1984	19V, 19H, 37V
ASI	ASI	Kaleschke et al. 2001	85V, 85H
Near 90GHz linear	N90	Ivanova et al., 2014	85V, 85H
One_channel (6H)	6H	Pedersen, 1994	6H
NASA Team 2	NT2	Markus and Cavalieri, 2000	19V, 19H, 37V, 85V, 85H
Eumetsat OSI-SAF*	?	Eastwood et al., 2012	Bristol, Bootstrap_f
SICCI*	?	Ivanova et al., 2015	Bristol, Bootstrap_f
Arctic Bootstrap*	?	Comiso et al., 1997; Comiso, 2009	Bootstrap_f, Bootstrap_p

1 Table 5. Statistical parameters of the comparison AMSR-E sea-ice concentration versus

2 MODIS sea-ice concentration (see Figure 4) for June 2009. Each column gives the value for

3 all grid cells with MODIS sea-ice concentration > 20%, the multiyear (MYI) ice grid cells and

4 the first-year ice (FYI) grid cells (see sub-section 2,.4). Slopes closed to 1, highest

5 correlations and lowest RMSD values are note by bold font.

June	Slope	Correlation	RMSD	N
Algorithm	All; FYI ; MYI	All; FYI; MYI	All; FYI ;MYI	All; FYI ;MYI
6H	1.16; 1.16; 1.19	**0.86; 0.89;** -0.28	17.1; 16.6; 18.8	6272; 1127; 649
ASI	*1.03; 1.05; 1.04*	*0.81; 0.86; -0.10*	*7.7; 10.3; 4.4*	
Bootstrap_f	1.27; 1.28; 1.28	0.72; 0.86; -0.50	27.9; 27.7; 30.2	
Bootstrap_p	0.92; 0.92; 0.97	0.62; 0.71; -0.01	13.9; 15.3; 9.0	
Bristol	1.14; 1.15; 1.16	0.75; 0.86; -0.42	16.3; 16.6; 18.6	
NASA-Team	**1.00; 1.01; 1.01**	0.71; 0.73; **0.32**	**8.9; 11.7; 6.3**	
Near90_lin	1.02; 1.03; 1.07	0.68; 0.81; -0.37	12.2; 13.0; 11.1	
NT2	*1.02; 1.04; 1.01*	*0.69; 0.79; 0.07*	*5.3; 8.5; 2.1*	

1   Table 6. Like Table 5 but for July 2009.

July	Slope	Correlation	RMSD	N
Algorithm	All; FYI ;MYI	All; FYI ; MYI	All; FYI ; MYI	All ; FYI ;MYI
6H	1.05; 1.08; 1.05	0.62; 0.81; -0.03	11.8; 12.4; 11.9	9612; 967; 634
ASI	*1.04; 1.09; 1.04*	*0.72; 0.83; -0.05*	*8.4; 11.8; 6.6*	
Bootstrap_f	1.12; 1.16; 1.13	0.55; 0.78; 0.14	18.1; 17.7; 20.1	
Bootstrap_p	0.90; 0.94; 0.90	0.62; **0.85**; -0.22	13.9; 9.9; 14.4	
Bristol	1.04; 1.08; 1.05	0.62; **0.85**; 0.05	11.7; 10.8; 12.0	
NASA-Team	0.97; **1.00**; 0.97	0.13; 0.80; -0.16	**10.3**; **8.9**; 10.4	
Near90_lin	**0.98**; 1.03; **1.00**	**0.63**; 0.82; 0.04	10.7; 10.9; **7.3**	
NT2	*1.04; 1.10; 1.02*	*0.66; 0.74;-0.03*	*7.4; 12.1; 5.7*	

1   Table 7. Like Table 5 but for August 2009.

August	Slope	Correlation	RMSD	N
Algorithm	All; FYI ; MYI	All; FYI ; MYI	All; FYI ; MYI	All ; FYI ;MYI
6H	1.08; **1.03**; 1.11	0.48; **0.62**; 0.22	10.0; 8.1; 11.0	5158; 162; 505
ASI	*1.13; 1.15; 1.14*	*0.55; 0.37; 0.25*	*12.5; 14.2; 13.0*	
Bootstrap_f	1.16; 1.15; 1.19	0.30; 0.49; 0.18	17.7; 15.4; 19.1	
Bootstrap_p	**1.00**; 0.95; **1.03**	0.27; 0.54; **0.44**	17.0; 8.8; **6.2**	
Bristol	1.10; 1.07; 1.13	0.46; 0.57; 0.35	12.0; 9.5; 12.8	
NASA-Team	1.03; 0.95; 1.06	0.48; 0.53; 0.31	**7.9**; **8.5**; 8.1	
Near90_lin	1.10; 1.07; 1.11	**0.54**; 0.35; 0.37	11.2; 11.2; 11.4	
NT2	*1.10; 1.14; 1.11*	*0.19; 0.15; 0.08*	*10.6; 13.8; 10.5*	

Table 8. Statistical parameters of the comparison AMSR-E sea-ice concentration versus MODIS ice-surface fraction for MODIS sea-ice concentration > 90% (see Figure 5) for June 2009. Each column gives the value for all grid cells with MODIS sea-ice concentration > 90%, and the respective multiyear (MYI) and first-year ice (FYI) grid cells

June	Slope	Correlation	RMSD	N
Algorithm	All; FYI ; MYI	All; FYI ; MYI	All; FYI; MYI	All ; FYI ; MYI
6H	1.23; 1.28; 1.22	0.40; 0.33;-0.14	22.6; 25.9; 21.9	5821; 916; 649
ASI	*1.09; 1.16; 1.07*	*0.09;-0.02;-0.01*	*10.8; 16.2; 7.6*	
Bootstrap_f	1.34; 1.43; 1.32	0.10; 0.36;-0.38	33.8; 38.3; 33.4	
Bootstrap_p	0.97; 1.02; 1.00	0.09;-0.10; 0.02	11.8; 13.9; 8.8	
Bristol	1.20; 1.28; 1.20	0.12; 0.22;-0.31	21.5; 25.8; 21.7	
NASA-Team	1.06; 1.11; 1.04	0.15;-0.15; 0.31	10.8; 16.0; 7.3	
Near90_lin	1.08; 1.15; 1.10	0.09; 0.05;-0.28	13.8; 17.1; 13.8	
NT2	*1.07; 1.14; 1.04*	*0.07;-0.08; 0.06*	*8.9; 14.2; 5.1*	

1   Table 9. Like Table 8 but for July 2009.

July	Slope	Correlation	RMSD	N
Algorithm	All; FYI ; MYI	All; FYI ; MYI	All; FYI; MYI	All ; FYI ; MYI
6H	1.34; 1.33; 1.33	0.82; 0.56; 0.84	26.8; 26.9; 26.5	7572; 491; 539
ASI	*1.30; 1.30; 1.29*	*0.43; 0.24; 0.36*	*25.8; 25.1; 26.5*	
Bootstrap_f	1.44; 1.42; 1.45	0.86; 0.65; 0.91	34.1; 33.7; 35.1	
Bootstrap_p	1.14; 1.15; 1.11	0.43; 0.15; 0.02	15.9; 15.9; 17.8	
Bristol	1.33; 1.32; 1.32	0.85; 0.65; 0.85	25.9; 25.8; 26.1	
NASA-Team	1.23; 1.21; 1.21	0.67; 0.26; 0.57	19.9; 19.4; 19.8	
Near90_lin	1.24; 1.26; 1.24	0.54; 0.33; 0.41	21.4; 22.6; 22.3	
NT2	*1.29; 1.28; 1.26*	*0.38; 0.36; 0.38*	*25.3; 23.7; 24.3*	

July	Slope	Correlation	RMSD	N
	All; FYI ; MYI	All; FYI ; MYI	All; FYI; MYI	All ; FYI ; MYI
6H	1.34; 1.33; 1.33	0.82; 0.56; 0.84	26.8; 26.9; 26.5	7572; 491; 539
Bootstrap_f	1.44; 1.42; 1.45	0.86; 0.65; 0.91	34.1; 33.7; 35.1	
Bootstrap_p	1.14; 1.15; 1.11	0.43; 0.15; 0.02	15.9; 15.9; 17.8	

1   Table 10. Like Table 8 but for August 2009.

August	Slope	Correlation	RMSD	N
Algorithm	All; FYI ; MYI	All; FYI ; MYI	All; FYI; MYI	All ; FYI ; MYI
6H	1.28; -- ; 1.30	0.39; -- ; 0.28	23.1; -- ; 24.2	2091; 44; 207
ASI	*1.33; -- ; 1.33*	*0.50; -- ; 0.65*	*26.8; -- ; 26.5*	
Bootstrap_f	1.36; -- ; 1.39	0.19; -- ; 0.19	30.3; -- ; 31.8	
Bootstrap_p	1.21; -- ; 1.25	0.14; -- ; 0.79	29.8; -- ; 19.4	
Bristol	1.31; -- ; 1.34	0.41; -- ; 0.51	25.3; -- ; 26.9	
NASA-Team	1.23; -- ; 1.26	0.49; -- ; 0.70	19.0; -- ; 21.0	
Near90_lin	1.32; -- ; 1.33	0.54; -- ; 0.68	25.4; -- ; 25.8	
NT2	*1.29; -- ; 1.29*	*0.18; -- ;-0.14*	*23.7; -- ; 23.6*	

1 Table 11. Top row: winter tie points for first-year ice (FYI) and multiyear ice (MYI)

2 expressed as normalized brightness temperature polarization difference PR; other rows:

3 summer tie points derived as outlined in the text expressed as PR and brightness temperature

4 (TB) at vertical (TBV) and horizontal (TBH) polarization. Brightness temperatures are given

5 together with one standard deviation.

Frequency	19 GHz	37 GHz	89 GHz
PR (winter, FYI;MYI)	0.030; 0.043	0.025; 0.031	0.021; 0.024
PR (summer)	0.034	0.033	0.021
TBH (summer) [K]	247.6 ± 6.5	239.0 ± 4.9	226.3 ± 10.0
TBV (summer) [K]	265.2 ± 2.5	255.5 ± 4.5	235.0 ± 11.8

1   Table 12. Slope of the linear relationship and correlation between AMSR-E sea-ice

2   concentrations and MODIS ice-surface fractions for the six algorithms, which do not cut-off

3   sea-ice concentrations, averaged over the six pentads July 11-15 to August 6-10. For each

4   algorithm, the average value ± 1 standard deviation (stddev), the range in the slope values and

5   the range in the correlations are given. (EV) denotes the explained variance. Case A60 and

6   A80 denote 100 % sea-ice concentration with 40% and 20% (apparent) open-water fraction

7   due to melt ponds, i.e. 60% and 80% ice-surface fraction, respectively. Case B60 and B80

8   denote 60% and 80% sea-ice concentration in case of 40% and 20% real open-water fraction,

9   i.e. ice-surface fraction = sea-ice concentration. A "*" indicates saturation, i.e. the retrieved

10   AMSR-E sea-ice concentration exceeds 100%. Bold numbers denote the maximum values for

11   mean slope and mean correlation.

Algorithm	6H	Bootstrap_f	Bootstrap_p	Bristol	NASA-Team	Near90_lin
Mean slope ± 1 stddev	1.36 ± 0.04	**1.44 ± 0.02**	1.24 ± 0.03	1.36 ± 0.02	1.29 ± 0.03	1.33 ± 0.03
Mean correlation ± 1 stddev (EV)	0.55 ± 0.16 (30%)	0.62 ± 0.10 (38%)	0.49 ± 0.14 (24%)	**0.68 ± 0.09 (46%)**	0.51 ± 0.10 (26%)	0.46 ± 0.20 (21%)
Slope range	1.29 to 1.41	1.41 to 1.47	1.21 to 1.29	1.34 to 1.39	1.26 to 1.32	1.29 to 1.38
Correlation	0.33 to 0.78	0.48 to 0.79	0.34 to 0.76	0.58 to 0.82	0.38 to 0.69	0.21 to 0.81
	Under-estimation of Case A / over-estimation of Case B sea-ice concentrations by the respective algorithm					
Case A60	-18.4%	-13.6%	-25.6%	-18.4%	-22.6%	-20.2%
Case A80	0.0% *	0.0% *	-0.8%	0.0% *	0.0% *	0.0% *
Case B60	+21.6%	+26.4%	+14.4%	+21.6%	+17.4%	+19.8%
Case B80	+20.0% *	+20.0% *	+19.2%	+20.0% *	+20.0% *	+20.0% *
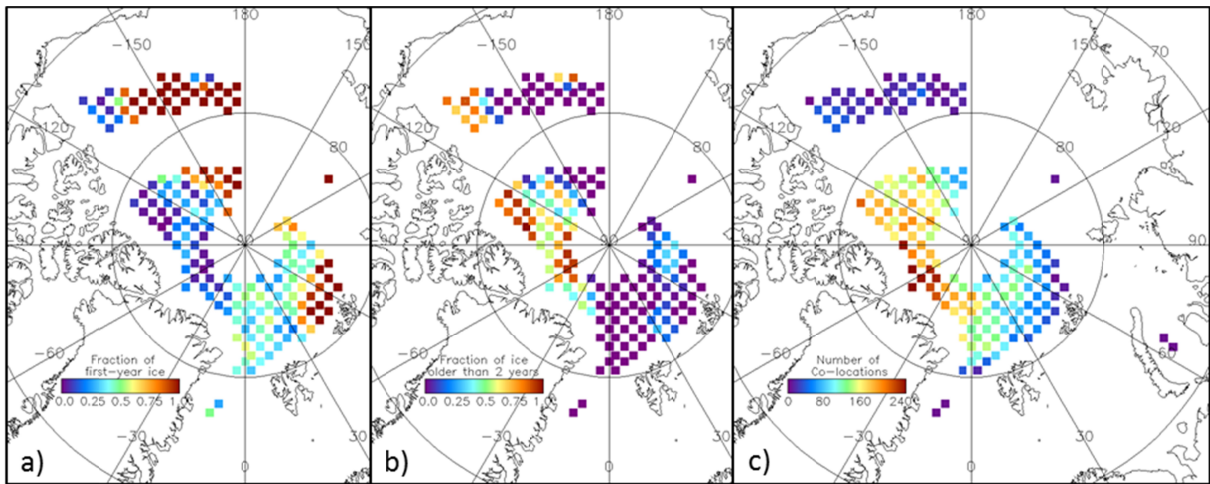
Figure 1. Spatial distribution of the MODIS sea-ice parameter data set super-posed with the fraction of first-year ice (a), multiyear ice (b), and the number of co-located daily MODIS sea-ice parameter data for the entire period June to August (c).
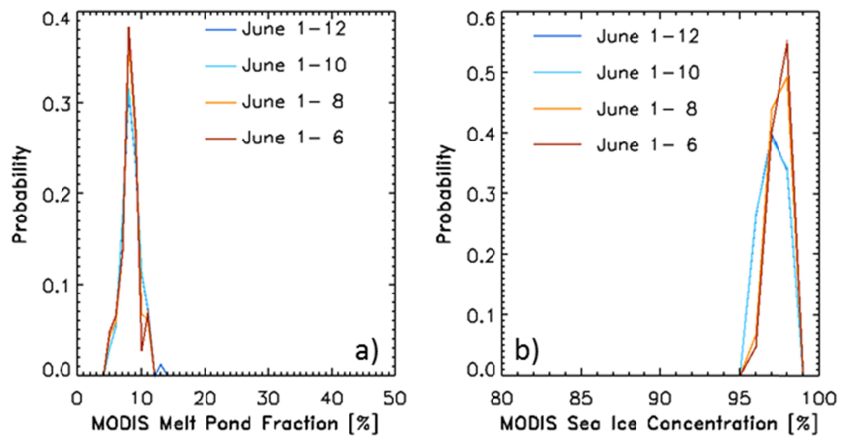
2 Figure 2. Histograms of MODIS melt-pond fraction (a) and MODIS sea-ice concentration (b)

3 derived when sea-ice cover was near 100% and melt ponds were not yet present (see text for

4 details) for the first 7, 9, 11, and 13 days of June 2009.
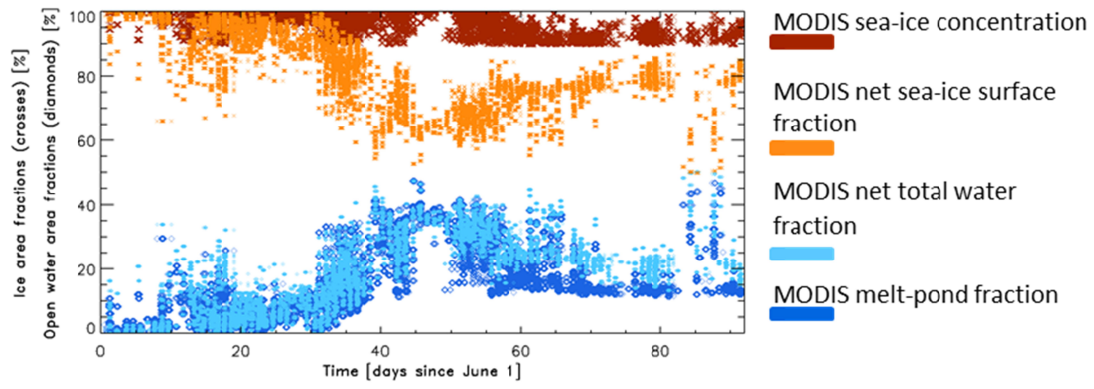
2   Figure 3. Time series of open water and sea-ice fractions for all MODIS grid cells used in the

3   present study for June 1, 2009 to August 31, 2009.
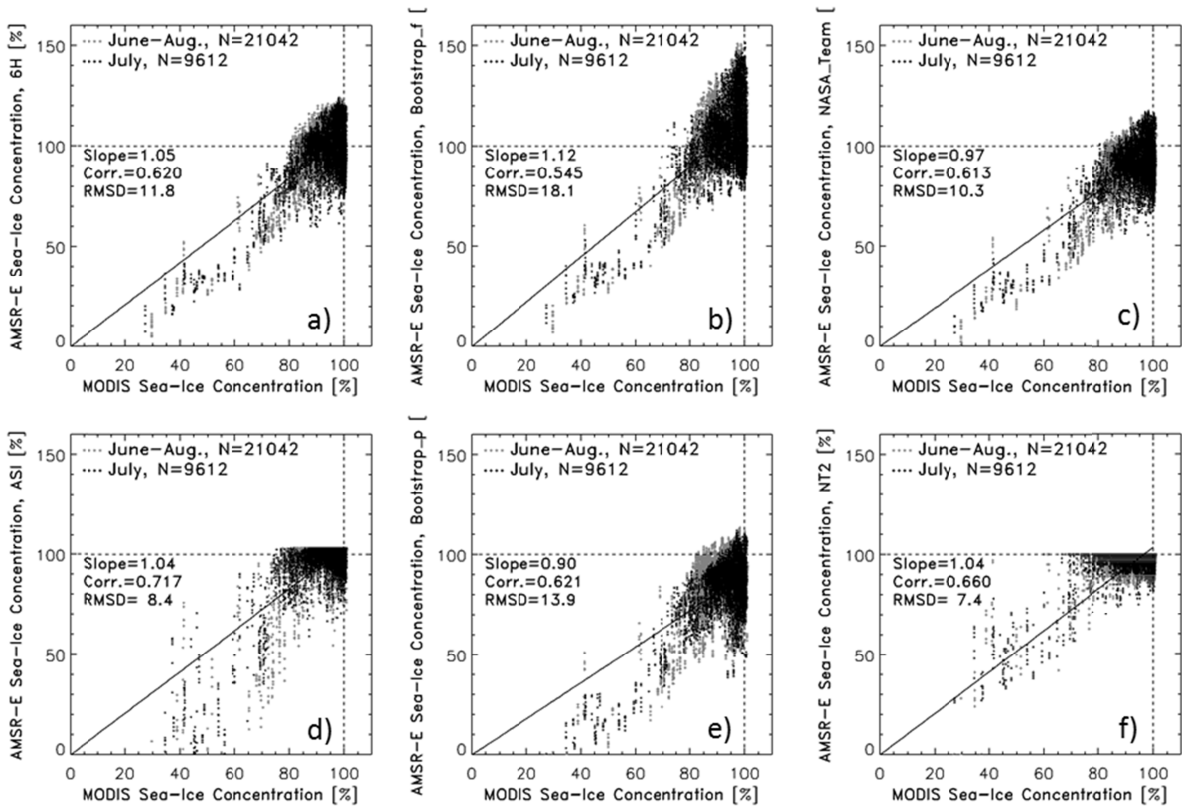
2   Figure 4. AMSR-E sea-ice concentration computed with 6 of the 8 algorithms listed in Table

3   2 versus MODIS sea-ice concentration for all grid cells with MODIS sea-ice concentration >

4   20%, and cloud fraction < 5%. Grey and black symbols denote data of the entire period and

5   July only, respectively. The black line denotes a linear regression of the sea-ice concentrations

6   of July forced through (0,0) with the slope as given in the each image. The linear correlation

7   coefficient and root mean squared difference for sea-ice concentrations of July are denoted by

8   "Corr." and "RMSD". Slope, Corr, and RMSD for June, July (this figure), and August are

9   summarized in Tables 5 to 7.
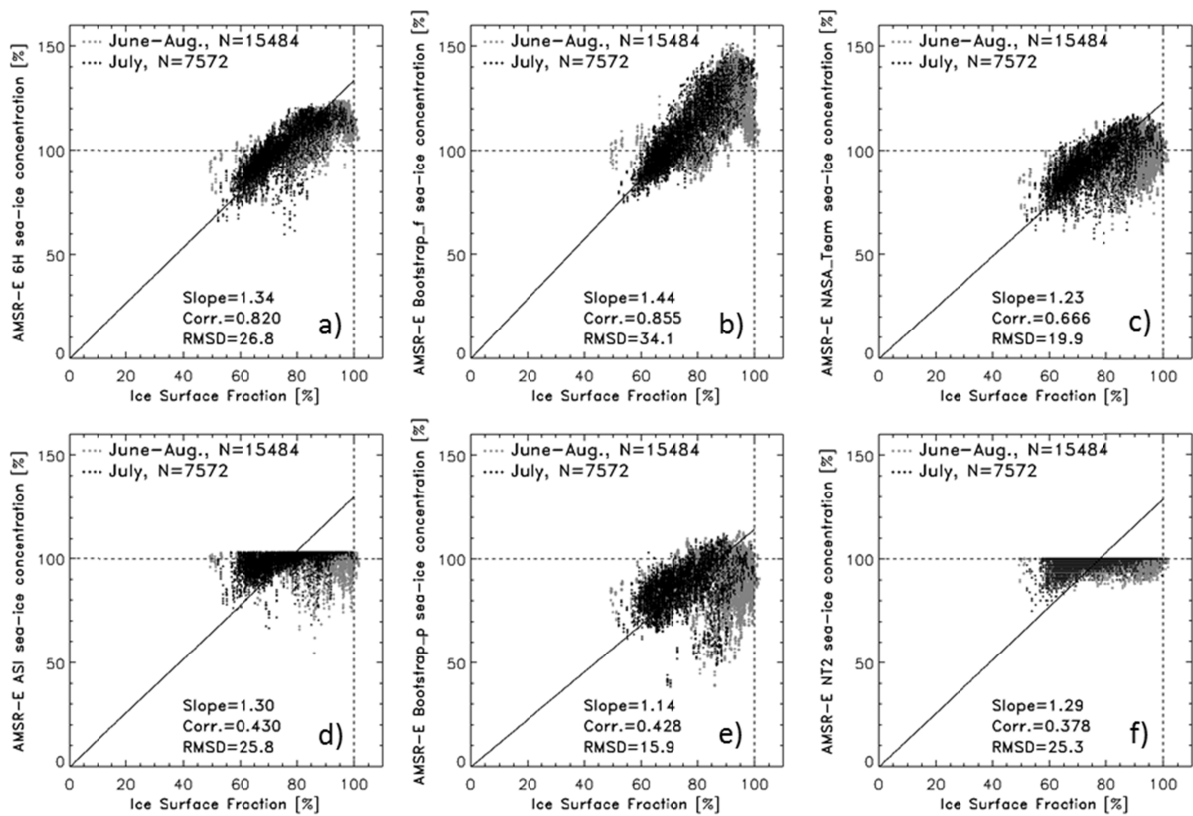
Figure 5. AMSR-E sea-ice concentration computed with 6 of the 8 algorithms listed in Table 2 versus MODIS ice-surface fraction for all grid cells with MODIS sea-ice concentration > 90%, and cloud fraction < 5%. Grey and black symbols denote data of the entire period and July only, respectively. The black line denotes a linear regression of the sea-ice concentrations of July forced through (0,0) with the slope as given in the each image. The linear correlation coefficient and root mean squared difference for sea-ice concentrations of July are denoted by "Corr." and "RMSD". Slope, Corr, and RMSD for June, July (this figure), and August are summarized in Tables 8 to 10.
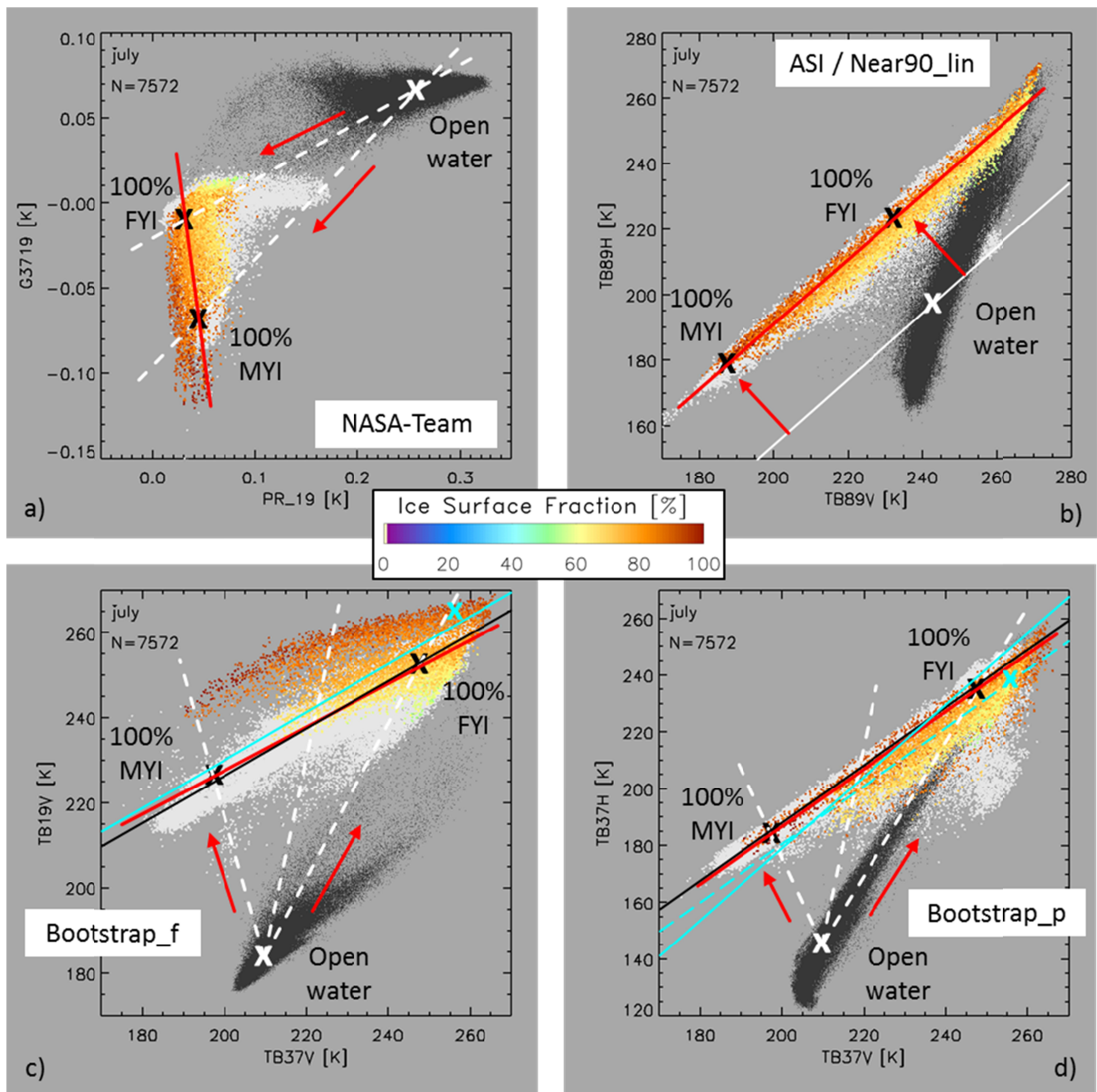
2   Figure 6. Parameter spaces for NASA-Team (a), ASI / Near90_lin (b), Bootstrap_f (c), and

3   Bootstrap_p (d) algorithms. Each image contains AMSR-E brightness-temperature data for

4   the respective space for July 2009, color coded with the contemporary MODIS ice-surface

5   fraction for cloud cover < 5% and MODIS sea-ice concentration > 90%. Black and white dots

6   denote winter (February 10, 2007) Arctic brightness temperatures for 0% and > 90 % NT2

7   sea-ice concentration, respectively. White and black crosses denote open water and sea-ice tie

8   points for winter, respectively (Ivanova et al., 2015). Red arrows direct into sea-ice

9   concentration increase. Red lines connect first-year ice (FYI) and multiyear ice (MYI) tie

10 points and are referred to as ice lines in the text. For white, black, and cyan lines and crosses

11 see text in sub-section 4.2.
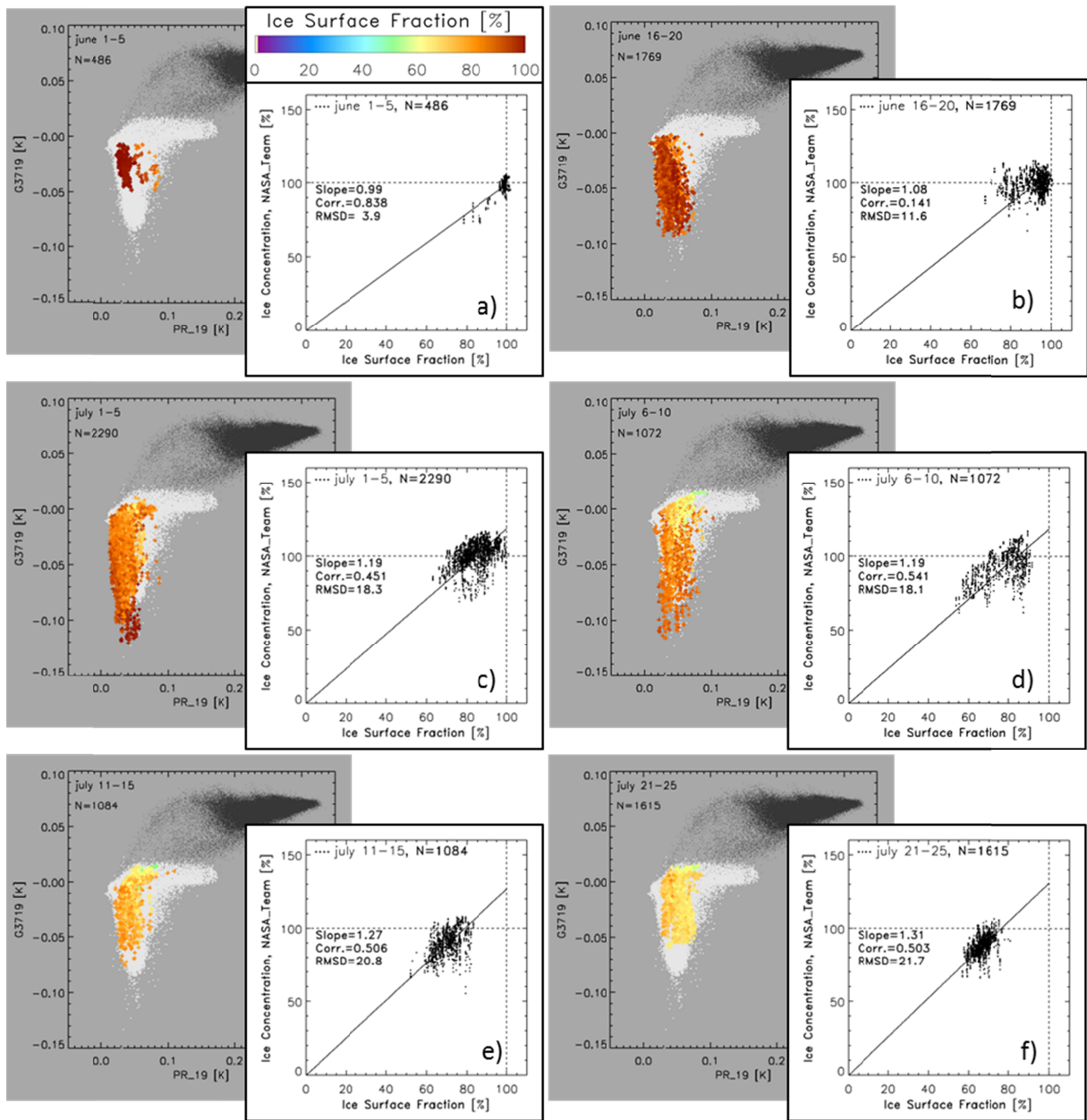
2 Figure 7. Background: AMSR-E brightness temperature frequency difference (gradient ratio,

3 GR) at 37 GHz and 19GHz, vertical polarization, versus AMSR-E brightness temperature

4 polarization difference (polarization ratio, PR) at 19 GHz, color-coded with the co-located

5 MODIS ice-surface fraction for 6 selected pentads denoted in the upper left corner of each

6 image together with the number N of data pairs. For white and black dots see Figure 6.

7 Foreground: NASA-Team sea-ice concentration versus MODIS ice-surface fraction for the

8 same pentads together with the linear regression line forced through (0,0). The slope of this

9 line is given together with the correlation between and the root mean squared difference

10 (RMSD) of the two data sets in each image.
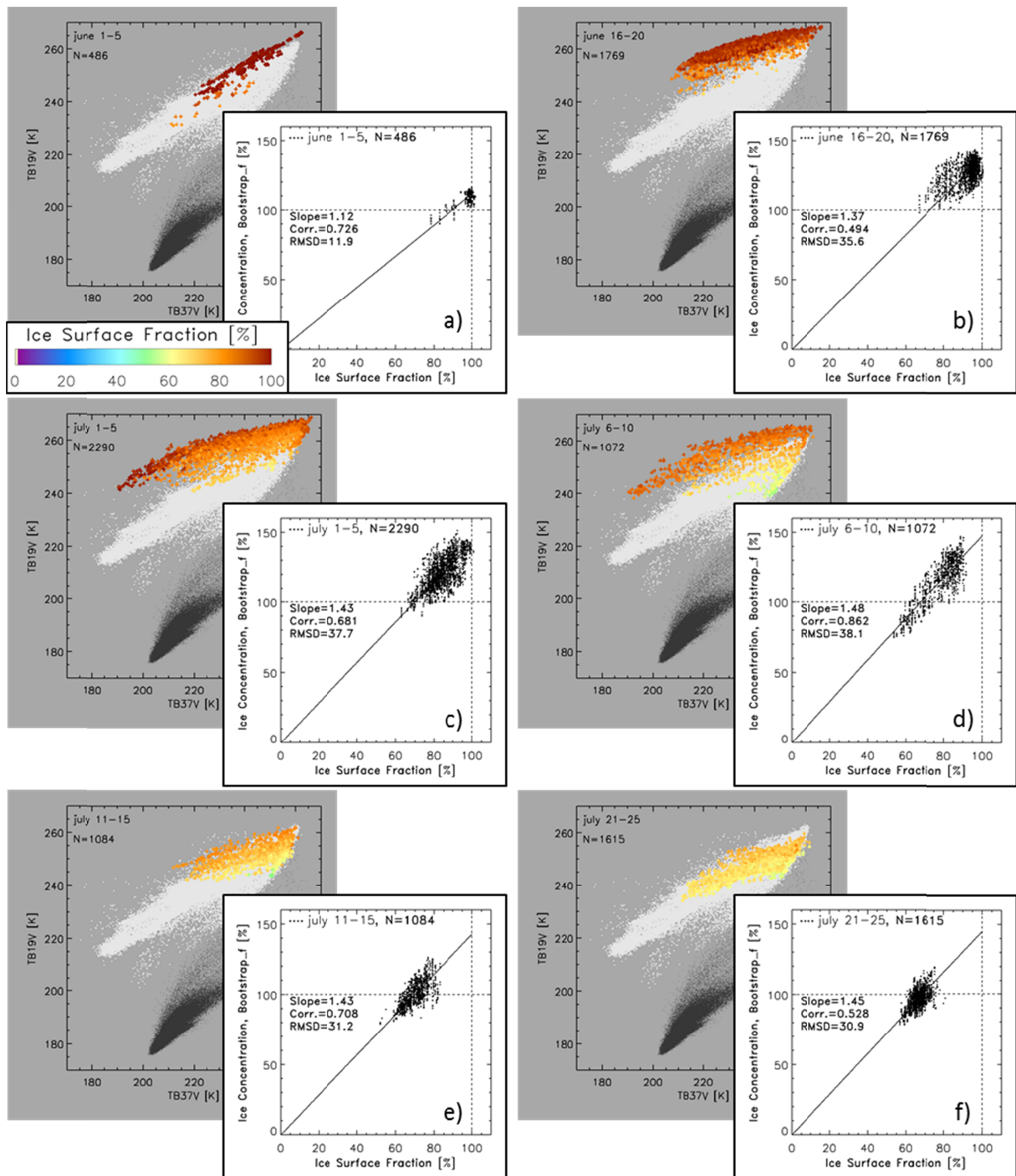
Figure 8. Background: Vertically polarized AMSR-E brightness temperature at 19 GHz and versus at 37 GHz, color-coded with the co-located MODIS ice-surface fraction for the same 6 selected pentads as in Figure 7 denoted in the upper left corner of each image together with the number N of data pairs. For white and black dots see Figure 6. Foreground: Same as in Figure 7 but for the Bootstrap_f algorithm.